DETERMINING THE OPTICAL PROPERTIES OF THE HUMAN BRAIN USING A TWO-LAYER DIFFUSION MODEL FOR NON-INVASIVE, FREQUENCY DOMAIN OPTICAL MEASUREMENTS

A thesis

submitted by

Elleesse Carlisle Navarro Pillas

In partial fulfillment of the requirements

for the degree of

Master of Science

In

Biomedical Engineering

TUFTS UNIVERSITY

May 2012

ADVISER: Sergio S. Fantini

Dedication

This work is dedicated to

Mama, Papa, Cathy and Jude

Acknowledgments

I am eternally grateful to the following people for making my studies at Tufts an intellectually enriching experience:

Sergio Fantini, my advisor, for his many helpful suggestions without which this project would not have been possible and his tireless patience during the many times when I seldom produced output.

Angelo Sassaroli for teaching me the rudiments of diffusion theory, Monte Carlo modeling and his valuable insight and guidance in the interpretation of results and establishing the algebraic system that allowed me to derive the solutions of the diffusion equation for the two-layer model.

Bertan Hallacoglu for generating the forward problem solver and his generosity in sharing his time in teaching me the ropes of MATLAB.

Abstract

Determining the optical properties of the human brain using a two-layer diffusion model for non-invasive, frequency-domain optical measurements

Elleesse Carlisle Navarro Pillas

The concentrations of oxyhemoglobin [HbO] and deoxyhemoglobin [Hb] in tissue and their temporal dynamics are an important indicator of cognitive function in the brain. Near-infrared (NIR) techniques have been employed to extract the concentration levels of these tissue chromophores due to their non-invasive feature. An integral part of this extraction procedure is a model of light propagation in turbid medium such as human tissue. In this study, we apply the diffusion model since the nature of light-tissue interaction for tissues probed with near-infrared light is highly scatter-dominated. In such a model of light propagation, the quantities of interest are the absorption μ_a and the scattering coefficient μ_s. From the absorption coefficients, the chromophore concentrations can be determined through their molar extinction coefficients. However, the model assumes a homogeneous issue structure and inevitably presents a limitation in the extraction process.

In this study, a two-layer model of the head is proposed to account for the heterogeneity in the tissue architecture of the head in recovering the absorption and reduced scattering coefficients (optical properties) of the brain. The model assumes a superficial layer of finite thickness (first layer) situated over a semi-infinite homogeneous structure (second layer). Applied to the head, the scalp and the skin are lumped together in the first layer and the brain comprises the latter. Values of intensity amplitude (AC) and phase (θ) are acquired in the frequency domain at multiple source-detector distances in a reflectance geometry. The optical properties are then recovered by performing a nonlinear regression to Monte Carlo-generated data for the AC and phase of the detected light. It is shown that the recovered optical properties

using this two-layer model exhibits better agreement with the simulations than those recovered from a homogeneous model.

The study hopes to provide an added avenue of refinement to a recent protocol that was developed to perform absolute measurements of cerebral hemoglobin concentration.

Contents

Dedication ii

Acknowledgments iii

Abstract iv

List of Tables viii

List of Figures ix

1 Introduction 1

1.1 Near-infrared spectroscopy (NIRS) 1

1.2 Measurement Techniques 3

1.2.1 Continuous Wave 3

1.2.2 Time Domain 4

1.2.3 Frequency Domain 5

1.3 Review of Selected Applications 6

1.3.1 Brain Activity 6

1.3.2 Glucose monitoring 7

1.3.3 Cancer Therapy 8

1.4 Outline 10

Chapter 1 References 12

2 Background and Theory 14

2.1 Introduction 14

2.2 Optical properties 15

2.2.1 Absorption coefficient (μ_a) 15

2.2.2 Scattering coefficient (μ_s) 16

2.2.3 The anisotropy factor (g) 16

2.2.4 The scattering phase function ($p(\cos\theta)$) 17

2.3 Modeling light transport 18

2.4 Absorption and scattering in the brain 21

2.4.1 Skin 21

2.4.2 Skull 22

2.4.3 Meninges 22

2.4.4 Cerebrospinal fluid 23

2.4.5 The brain 23

2.5 The two-layer model 24

Chapter 2 References 29

3 Determination of the Optical Properties of a Two-layered Medium as a Model of the Head 32

3.1 The Monte Carlo approach 32

3.2 Forward modeling 36

3.3 Results 42

3.3.1 Recovering μ_{a1} and μ'_{s1} 42

3.3.2 Recovering μ_{a2} and μ'_{s2} 45

3.3.3 Sensitivity to errors in l, μ_{a1} and μ'_{s1} 47

3.4 Discussion 49

3.5 Conclusion and future directions 51

Chapter 3 References **53**

Appendix A: Derivation of the solutions to the diffusion equation for a two-layered turbid media 56

Appendix B: The Limiting Equation **66**

List of Tables

1 Reduced scattering coefficients (μ_s') of select biological tissues 18

2 Optical properties of grey and white matter 24

3 Optical properties for a two-layer medium with a top layer thickness of 5mm and 10mm 41

4 Sensitivity of the recovery of the bottom layer's optical properties to errors in l, μ_{a1} and μ_{s1}' for a top layer thickness of 5mm 48

5 Sensitivity of the recovery of the bottom layer's optical properties to errors in l, μ_{a1} and μ_{s1}' for a top layer thickness of 10mm 48

List of Figures

1 Absorption of the various tissue chromophores 1

2 Incident and outgoing intensity profile of a continuous wave (CW) source as a function of time 3

3 Time domain intensity profile of incident and outgoing light as a function of time 4

4 Intensity profile of incoming and outgoing light for a sinusoidally-modulated source 5

5 Source and detector probe arrangement in a reflectance geometry 6

6 Variation in the reduced scattering coefficient (μ_s') in response to induced changes in blood glucose concentration 7

7 Diffuse correlation spectroscopy as applied to the human breast 9

8 Activation of a photosensitive agent (Photofrin) delivered to a murine tumor 10

9 Diffuse correlation spectroscopy as applied to photodynamic therapy of the human prostate 10

10 Partial reflection and transmission of light based on Snell's law 14

11 Change in the direction of travel for a photon undergoing scattering 17

12 Turbid medium as a semi-infinite medium employing the extrapolated boundary condition 20

13 Comparison between reflectance predicted by Monte Carlo simulations and diffusion theory 20

14 Anatomical cross-section of the skin 21

15 Bones of the skull and its architecture 22

16 The Meninges 23

17 Anatomy of a neuron 24

18 Two-layer model of the human head 26

19 Comparison between the intensity amplitude (AC) and phase predicted by Monte Carlo simulations and the two-layer model for a superficial layer thickness of 5mm 37

20 Comparison between the intensity amplitude (AC) and phase predicted by Monte Carlo simulations and the two-layer model for a superficial layer thickness of 10mm 38

21 Comparison between reflectance profile predicted by the two-layer model and the homogenous model representative of the top and bottom layer for a top layer thickness of 5mm and 10mm 39

22 Steps in recovering the optical properties of the bottom layer (brain) 42

23 Estimated absorption coefficient of the first layer of a two-layer medium with a top layer thickness of 5mm 43

24 Estimated reduced scattering coefficient of the first layer of a two-layer medium with a top layer thickness of 5mm 44

25 Estimated absorption coefficient of the first layer of a two-layer medium with a top layer thickness of 10mm 44

26 Estimated reduced scattering coefficient of the first layer of a two-layer medium with a top layer thickness of 10mm 45

27 Values of the absorption coefficient of the bottom layer of a two-layer medium recovered by a two-layer model and a homogenous model for a top layer thickness of 5mm 46

28 Values of the reduced scattering coefficient of the bottom layer of a two-layer medium recovered by a two-layer model and a homogenous model for a top layer thickness of 5mm 46

29 Values of the absorption coefficient of the bottom layer of a two-layer medium recovered by a two-layer model and a homogenous model for a top layer thickness of 10mm 47

30 Values of the reduced scattering coefficient of the bottom layer of a two-layer medium recovered by a two-layer model and a homogenous model for a top layer thickness of 10mm 47

Chapter 1: Introduction

1.1 Near-infrared Spectroscopy (NIRS)

Near-infrared spectroscopy (NIRS) is a method used in studying the optical properties of a given medium using wavelengths of light in the range (600-1000nm). These properties are related to the medium's ability to absorb and scatter light. Applied to human tissue, compounds that exhibit absorption for a given wavelength are called chromophores (Fig.1). [1] In the near infrared wavelength region, scattering is the dominant mode of interaction of light with biological tissue. Absorption, on the other hand, is notably low in the near-infrared thereby allowing the incident light to travel at greater depths. For measurements aimed at investigating the optical properties of tissue, a defining feature of NIRS is its non-invasive nature. In such measurements, the quantities of interest are the absorption (μ_a) and reduced scattering (μ_s') coefficients. In diagnostic settings, these turn out to be important biological markers in assessing the physiological state of tissue. For instance, the changes in the absorptive properties associated with cyclic variations in tissue perfusion allows for the investigation of tissue hemodynamics. The primary absorber at the short end of the spectrum is hemoglobin in both its deoxygenated and oxygenated state whereas water absorption is more pronounced in the IR region.

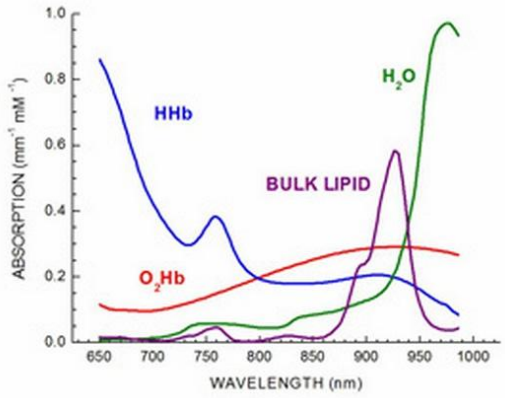

Figure 1 Absorption of the various tissue chromophores.

Studies[2] employing light sources in the near-infrared (NIR) domain have been conducted where oxygen saturation was determined from concentration levels of deoxyhemoglobin [Hb] and oxygenated hemoglobin [HbO]. These physiological parameters are deduced from μ_a. The amount of these chromophores can be quantified by using an expression that relates their concentration to the absorption coefficient of the medium being investigated. For example, the concentration of oxygenated [HbO] and deoxygenated [Hb] hemoglobin can be calculated by measuring the absorption coefficient at two distinct wavelengths in the near-infrared range[3]:

$$\mu_a(\lambda_1) = \varepsilon_{\mathrm{Hb}}^{\lambda_1} * [\mathrm{Hb}] + \varepsilon_{\mathrm{HbO}}^{\lambda_1} * [\mathrm{HbO}] \tag{1.1}$$

$$\mu_a(\lambda_2) = \varepsilon_{\mathrm{Hb}}^{\lambda_2} * [\mathrm{Hb}] + \varepsilon_{\mathrm{HbO}}^{\lambda_2} * [\mathrm{HbO}] \tag{1.2}$$

Where ε is the molar extinction coefficient of a chromophore for a certain value of the wavelength and is expressed in units of mm^{-1}/Mol and μ_a is the absorption coefficient given in units of mm^{-1}. Often, the effective values of these optical properties are determined using a model of light propagation that assumes a homogeneous medium. However, as this study will later expound upon, the heterogeneous structure of tissue presents a limitation to the applicability of the homogeneous model in accurately extracting μ_a and μ_s'. This section reviews NIRS measurement techniques and the applications to which NIRS has been used in recovering μ_a and μ_s' using a homogenous model of human tissue.

1.2 Measurement Techniques

1.2.1 Continuous Wave

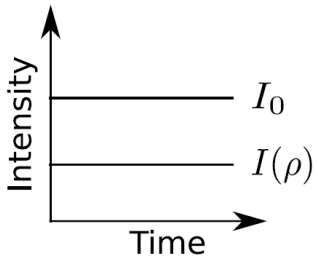

Figure 2 Intensity of incoming (I_o) and outgoing ($I(\rho)$) light after traversing an attenuating medium, where ρ(mm)s is the source-detector separation. (Image reproduced from Ref.[4])

Continuous wave (CW) techniques make use of light sources whose intensity output is constant. When a medium is illuminated with a CW source, the intensity of the outgoing light allows one to account for the intensity that has been lost due to attenuation of the incident light(Fig. 2).[4] In a reflectance configuration, where the light source and the detector are on the same side of the medium being examined, different areas can be investigated by tailoring the wavelength of the CW source. For example, by employing wavelengths in the range 500-600nm, one gains sensitivity to hemodynamic changes occurring in superficial blood vessels whereas deeper regions can be explored by using wavelengths >700nm [5].

To determine the optical properties of a medium, several models and methods have been employed to describe the nature of light propagation in turbid media; Kubelka-Munk theory[5],[6], adding-doubling method[6], two-flux approach [5],[7]. In these models, however, the respective expressions for the diffuse reflectance involve either products or ratios of the optical properties and thus cannot be separated. This apparent shortcoming is circumvented by employing source-detector separations that minimizes the partial contribution of the medium's scattering properties to the collected signal. In this way, the loss in the intensity of the outgoing light can be attributed mainly to absorption [5].

An important application to which CW techniques has been used include the characterization of skin lesions.[8],[9],[10]

1.2.2 Time Domain

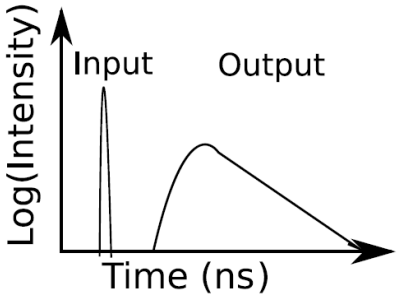

Figure 3 In the time domain, a narrow input beam exits an attenuating medium in a broadened form. (Image reproduced from T. Durduran *et al.* 2011)

Time domain measurements employ periodically pulsed light sources. Once delivered to a highly scattering medium, the pulse widens before arriving at the detector (Fig. 3). In this broadened form, the medium's optical properties can be deduced. The measured quantity in the time domain is the time of flight for each detected photon.[4],[5] In studying thin samples, techniques such as time-gating can be employed to bias the collected of transmitted photons that have propagated mainly in the forward direction.[4] This technique accepts photons whose duration of travel in the medium falls within a given time interval. For high photon populations, however, determining the time-of-flight of each photon translates to a longer data acquisition period.[5]

1.2.3 Frequency Domain

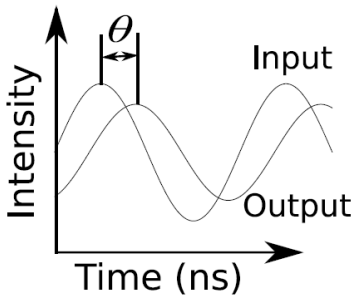

Figure 4 A phase difference is observed between incident and outgoing light that is sinusoidally-modulated. (Image reproduced from Durduran *et al.* 2011)

For measurements performed in the frequency domain (FD) (Fig.4), the modulation of light permits the collection of signals that are characterized by various sinusoidal components.[5] Three parameters can be defined that describe the total intensity *I* (expressed in units of power per unit area) of the input: the DC intensity (I_{DC}), the AC intensity (I_{AC}) and the phase (θ) expressed in units of radians,

$$I = I_{DC} + I_{AC}\cos(\theta - \omega t) \tag{1.3}$$

In a typical measurement scenario, a source probe is placed in contact with the medium of interest and illuminates it (Fig. 5). At a different point on the surface of the medium, a detector probe collects light that has traveled a certain distance from the source. It should be noted that the same relationship, Eq (1.3), is valid for the intensity of detected light I_d where both its DC and AC components exhibit an exponential attenuation with ρ,

$$I_d(\rho, t) = \frac{S}{4\pi D\rho}\{I_{DC}(\rho) + I_{AC}(\rho)\cos(\theta_d - \omega t)\} \tag{1.4}$$

Where ρ is the source-detector separation; $I_{DC}(\rho) = I_{DC}e^{-\rho\sqrt{\mu_a/D}}$; $I_{AC}(\rho) = I_{AC}e^{-k\rho}$; D is the diffusion coefficient, defined as $\frac{1}{3(\mu_a+\mu_s')}$; $k = \sqrt{\frac{c\mu_{a-i\omega}}{cD}}$, where $\omega = 2\pi f$ and f is the frequency of modulation; c is the speed of light in the medium; $i = \sqrt{-1}$ and θ_d is the phase difference between the incident and detected light (increases linearly in ρ).

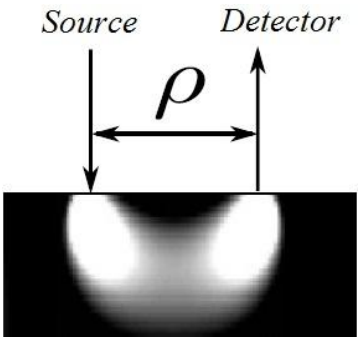

Figure 5 Configuration of source and detector probes for measurements made in a reflectance geometry. (Image reproduced from Durduran *et al.* 2011)

Compared to time-domain techniques, where the total time of flight is measured for each detected photon, FD permits faster data acquisition.[5] In contrast to CW techniques, FD measurements are able to separate scattering and absorption contributions to the collected light. [5]

1.3 Review of Selected Applications

1.3.1 Brain activity

The link between variations in oxygenated hemoglobin [HbO], deoxygenated hemoglobin [Hb] and cerebral activity has been exploited to examine regional brain activation under the influence of an external stimulus. Finger tapping experiments, for instance, was performed in both the frequency and time domains to examine the changes in perfusion affecting the motor cortex contralateral to the tapping limb.[11] In the same study, the viability of separating the contributions of what are termed as fast effects from slow ones in the collected optical signal was investigated as well. Measurements were carried out in the frequency domain using the multi-distance method to tease out the fast changes associated with fluctuations in μ_s' – occurring on the order of milliseconds (ms) for the stimulation protocol used – which is often buried in an optical signal dominated by absorption changes. Stimulation of the visual cortex was carried out to determine the fast changes in μ_s'. In contrast to the hemodynamic origins of slow effects, fast effects have been attributed to neuronal activity.[12] Evidence for this comes from measurements made on exposed cortex of animals.[13]

These developments could aid in concurrent studies that aim to determine regions of the brain that operate together under the influence of a stimulus by examining the time of onset of the changes in optical parameters.

1.3.2 Glucose monitoring

The influence of blood glucose levels on the scattering properties of tissue has been studied.[14] The reduced scattering coefficient (μ_s') can be attributed to local variations in the index of refraction for a given medium. A mismatch in the refractive index between extracellular fluid and immersed structures in it provided a means of investigating the possible correlation between blood glucose concentrations and μ_s'. Glucose was introduced in incremental steps to a diabetic volunteer and the concentration was monitored using a Biostat. Measurements were collected on the abdomen. A reduction of the refractive index mismatch due to the presence of glucose in the blood was observed (Fig. 6). This translated to a decrease in the reduced scattering coefficient. Insulin was then injected to re-establish normal blood glucose levels and μ_s' was restored to its value prior to glucose administration.

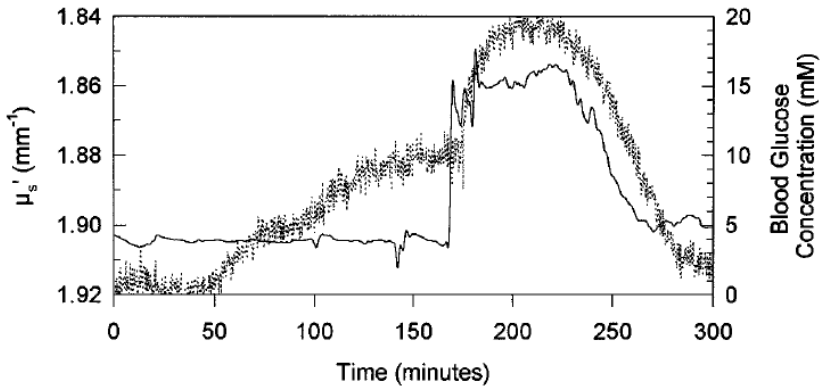

Figure 6 A decrease in the reduced scattering coefficient is observed under increased glucose concentration levels. (Reproduced from Bruulsema *et al.*1997)

Results from this study may find clinical application to monitor blood glucose levels non-invasively. This would be of great benefit to diabetic patients who routinely receive insulin shots to maintain and monitor normal blood glucose levels.

1.3.3 Cancer Therapy

An emerging technology drawing upon the success of NIR techniques is diffuse correlation spectroscopy (DCS). It measures the movements of red blood cells (RBCs) from fluctuations in the collected NIR light and has been used to analyze blood flow. Its performance as a potential diagnostic and therapeutic tool in cancer studies has been investigated[15]; in the diagnostic realm, DCS/NIRS has been employed to differentiate between the metabolic rates of oxygen of patients that were known to have breast tumors ($TMRO_2$) from those with healthy breast tissue. The contrast between these two tissues was achieved by measuring the relative blood flow among a total of seven subjects using an optical probe. Five of these subjects were known to carry tumors in their breasts whereas the remaining two did not. Measurements were performed by scanning a handheld optical probe horizontally and vertically. Two scan directions were made to ensure reproducibility of the measurements. For each scan direction, the breast was scanned in 1cm increments. The figure below illustrates the scanning configuration (Fig. 7a) and the regional blood flow (rBF) obtained from the two scanning directions (Fig. 7b and 7c). The increased blood flow associated with tissues that are known to harbor malignant tissue masses such as tumors illustrates the sensitivity of DCS to these physiological processes. Furthermore these results were in agreement with Doppler ultrasound and PET studies that were carried out in the same study.

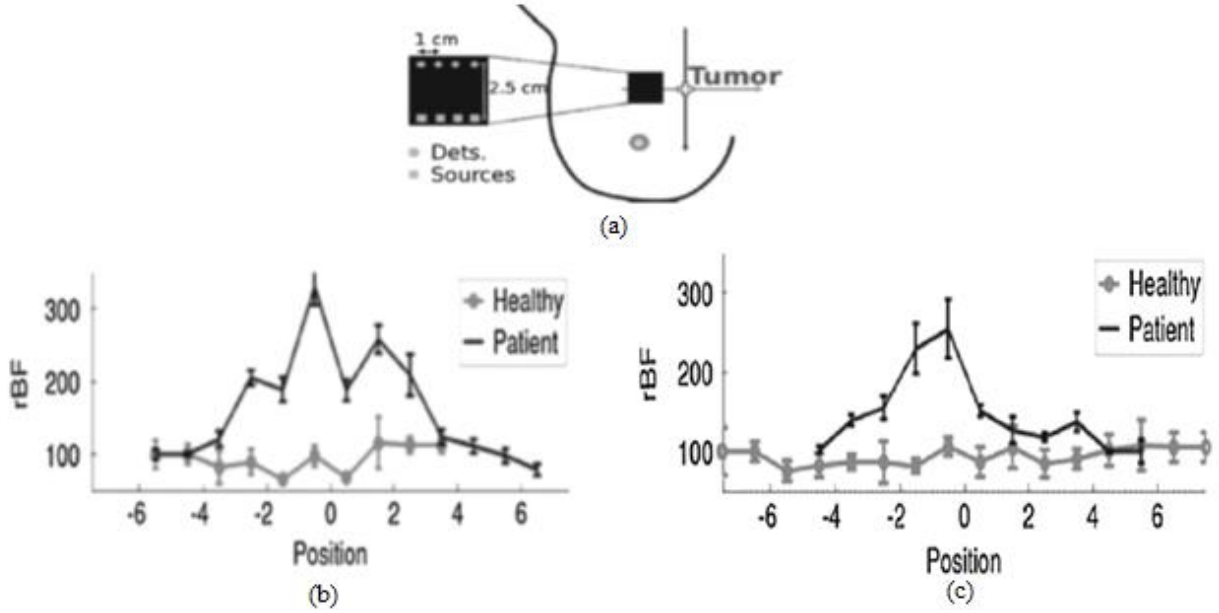

Figure 7 (a) The breast is scanned with a handheld probe in the horizontal and vertical directions in steps of 1cm. Representative regional blood flow (rBF) measurements as a function of position obtained from one patient with a breast tumor and one healthy subject in the horizontal (b) and vertical (c) direction.

In addition, the prospective utility of DCS in assessing the efficacy of cancer therapies was also explored. Measurements on monitoring the relative blood flow (rBF) in murine tumors treated with Photofrin was performed prior to, during, and after light activation. Blood flow was seen to increase within the first few minutes after activation. After attaining a peak value, blood flow exhibited a decline eventually reaching a minimum that was ~50% below its value prior to illumination. The results obtained support the claim that reduction of tumor oxygen supply was a marker of Photofrin's photoactivity (Figure 8).

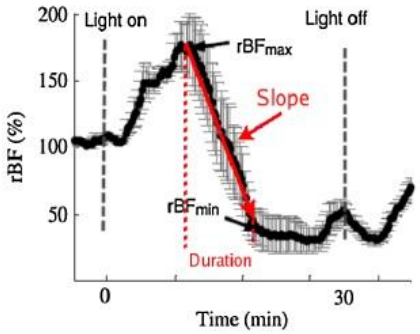

Figure 8 Activation of Photofrin in murine tumor under illumination (Reproduced from Yu *et al.* 2012)

These results were then extended to studies that monitored the human prostate during the photodynamic therapy (PDT). Five subjects with prostate cancer were used for the study. Using, a fiber optic probe, four quadrants of the prostate were illuminated and examined for blood flow changes in motexafin lutetium (MLu)-based PDT. Similar to results obtained in murine tumors, the photoactivation of MLu in the prostate induced a reduction in rBF. For the five subjects, this reduction was -41%±12%. (Figure 9)

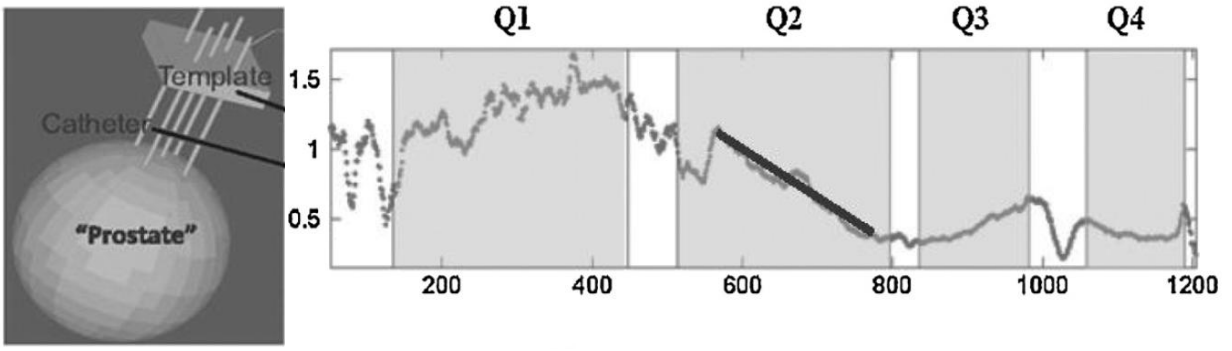

Figure 9 Reduction in relative blood flow upon photoactivation of MLu in Quadrant 2. Four quadrants of the prostate were illuminated. (Reproduced from Yu *et al.* 2012)

1.4 Outline

This study investigates the determination of the optical properties of the brain using a two-layer model of human tissue as first put forth by Alwin Kienle (1998).[16] Chapter 2 delves into the theory of light propagation in a highly scattering medium; the optical properties are defined and the diffusion equation is introduced. In the same chapter, a description of the two-layer model is also given. Chapter 3 deals with

the steps involved in the inversion procedure employed in determining the optical properties of the brain. The values of μ_a and μ_s' obtained from using the solution of the two-layer diffusion model are then presented followed by a discussion of the results.

Chapter 1 References

[1] P. Prasad, Introduction to Biophotonics (John Wiley & Sons, Inc. Hoboken, New Jersey, 2003)

[2] J. Zhao, H. Ding, X. Hou, C. Zhou, and B. Chance, ”In vivo determination of the optical properties of infant brain using frequency-domain near-infrared spectroscopy,” Journal of Biomedical Optics **10**(2), 024028, 1-7 (2005).

[3] L. Wang and H. Wu, Biomedical Optics: Principles and Imaging (John Wiley & Sons, Inc. Hoboken, New Jersey, 2003) Chapter 1.

[4] T. Durduran, R. Choe, WB Baker, and AG Yodh, ”Diffuse optics for tissue monitoring and tomography,” Rep. Prog. Phys. **73** (2010)

[5] E. Gratton and S. Fantini, "Reflectance and transmittance spectroscopy," in Lasers and current optical techniques in biology," Comprehensive Series in Photochemistry and photobiology," Vol. 4, G. Palumbo and R. Pratesi, Editors, (Royal Society of Chemistry, Cambridge, UK, 2004), pp. 211-258

[6] A. Ishimaru, Wave Propagation and Scattering in Random Media (Academic, New York, 1997).

[7] A. Bashkatov, E. Genina, V. Tuchin, ”Tissue Optical Properties,” in Handbook of Biomedical Optics, David, C, Pitris, and N. Ramanujam, Editors (CRC Press,2011), pp.67-100

[8] R. Marchesini, S. Tomatis, C. Bartoli, A. Bono, C. Clemente, C. Cupeta, I. Del Prato, E. Pignoli, A.E. Sichirollo, N. Cascinelli,”In vivo spectrophotometric evaluation of neoplastic and non-neopastic skin pigmented lesions.III.CCD camera-based reflectance imaging.” Photochem. Photobiol. **62**, 151-154 (1995).

[9] B. Farina, C. Bartoli, A. Bono. A. Colombo, M. Lualdi, G. Tragni, and R. Marchesini,"Multispectral imaging approach in the diagnosis of cutaneous melanoma: potentiality and limits," Phys. Med. Biol. **45**,1243-1254 (2000).

[10] A. Garcia-Uribe, E. Smith, J. Zhou, M. Duvic, V. Prieto, L. Wang,"In vivo characterization of optical properties of pigemented skin lesions incuding melanoma using oblique incidence diffuse reflectance spectrometry," Journal of Biomedical Optics Letters, **16**(20), 020501,1-3 (2011).

[11] E. Gratton, S. Fantini, M. A. Franceschini, G. Gratton, and M. Fabiani, "Measurements of Scattering and Absorption Changes in Muscle and Brain," Phil. Trans. R. Soc. of Lond. B **352**, 727-735 (1997).

[12] Y. Hoshi and M. Tamura, "Dynamic multichannel near-infrared optical imaging of human brain activity," J. Appl. Physiol. **75**, 1842-1846 (1993).

[13] R.D. Frostig, E.E. Lieke, D.Y. Ts'o and A. Grinvald, "Cortical functional architecture and local coupling between neuronal activity and the microcirculation revelard by in vivo high-resolution optical imaging of intrinsic signals," Proc. Natn. Acad. Sci, USA **87**, 6082-6086 (1990).

[14] J.T. Bruulsema, J.E. Hayward, T.J. Farrell, M.S. Patterson, L.Heinemann, M. Berger, T. Koschinsky, J. Sandahl-Christiansen, H. Orskov, M. Essenpreis, G. Schmelzeisen-Redeker, and D. Böcker,"Correlation between blood glucose concentration in diabetics and noninvasively measured tissue optical scattering coefficient," Optics Letters **22**(3),190-192 (1997).

[15] G. Yu,"Near-infrared diffuse correlation spectroscopy in cancer diagnosis and therapy monitoring," Journal of Biomedical Optics **17**(1), 010901, 1-9 (2012).

[16] A. Kienle, T. Glanzmann, M.S. Patterson, N. Utke, R. Bays, G. Wagniéres, and H. van der Bergh, "Noninvasive determination of the optical properties of two-layered turbid media," Appl. Opt. **37**, 779-791 (1998).

Chapter 2: Background and Theory

2.1 Introduction

The propagation of light in a turbid medium is governed by absorption and scattering events which, together, lead to an overall attenuation of the incident light. A reduction in the intensity of light due to absorption is a consequence of energy transfer between the incoming light and the absorbing elements of the medium. The contribution of scattering to losses in the intensity originates from interactions that deflect the incoming light from its original direction of travel. When light deflected by a particle possesses the same energy it had prior to collision, the scattering event is said to be elastic.[1] On the other hand, the interaction is inelastic when light imparts a fraction of its energy during collision. In addition, for a complex medium characterized by internal boundaries between different structures, a mismatch in the index of refraction also contributes to attenuation through the partial reflection and transmission of light. [1],[2] An illustration of this phenomenon from geometric optics is shown below for an interface between two domains with different indices of refraction:

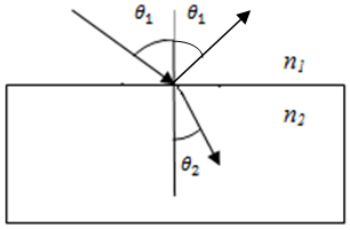

Figure 10 Light incident on an interface that separates two media differing in their refractive index is refracted according to Snell's law.

The diffusion approximation to the more rigorous radiative transport equation (RTE) has proven to be a viable model in describing the behavior of light in tissue-mimicking phantoms and has been investigated extensively in the near-infrared region. Diffusion theory treats light as a stream of photons, each undergoing random collisions as they traverse the volume of a host medium where they are either scattered, absorbed or lost through the boundary of the medium.[3] The mathematical equation describing the nature of light-tissue interactions in this region of approximation is called the diffusion equation (DE).

When the boundaries are regular, the DE can be solved analytically for the desired tissue geometry (e.g. slab, semi-infinite, cylindrical, spherical etc.) by imposing appropriate boundary conditions. For more complex geometries, however, one must resort to numerical methods such as finite-element method (FEM).[4] The solutions can then be used to determine the intensity of the attenuated light that was either transmitted or reflected.

2.2 Optical properties

2.2.1 Absorption coefficient (μ_a)

When a plane wave carrying intensity *I* (Power per unit area) impinges on an absorbing particle, the ratio of the power absorbed by the particle P_a to the incident intensity *I*, we define the absorption cross section σ_a as:

$$\sigma_a = \frac{P_a}{I} \tag{2.1}$$

For a medium populated by absorbing particles, it is convenient to define the space occupied by these particles in terms of the volume density (ρ_a). This quantity gives the number of absorbing particles per unit volume of the host medium. The absorption coefficient then follows from the two quantities previously described:

$$\mu_a = \rho_a \sigma_a \tag{2.2}$$

Its reciprocal is given by $\langle l_a \rangle = 1/\mu_a$ and it stands for the mean free path traveled by a photon before being absorbed.[5] Note that Eq.(2.2) considers only the absorption from a particle in a medium; however absorption can also occur in the background medium.

2.2.2 Scattering coefficient (μ_s)

For scattered light, we define the scattering cross section σ_s as:

$$\sigma_s = \frac{P_s}{I} \tag{2.3}$$

Where P_s is the power scattered by on particle and I is the incident intensity.

The number of scattering particles per unit volume is likewise given by ρ_s. An expression for the scattering coefficient is then given by:

$$\mu_s = \rho_s \sigma_s \tag{2.4}$$

Its reciprocal, given by $\langle l_s \rangle = 1/\mu_s$ represents the average distance traveled by a photon before two consecutive scattering events.[5] It is important to note that Eq. (2.4) is only true for "low" (few %) particle concentration.[6]

2.2.3 The anisotropy factor (g)

The degree by which incident light changes its direction of travel due to scattering interactions is described by the anisotropy factor. This quantity is defined by the average value of the cosine of the angle between the incoming and scattered light, traveling in directions $\boldsymbol{s}$ and $\boldsymbol{s'}$ respectively. From this description, it follows that the possible values spanned by g lie between -1 and 1; a value of -1 corresponds to backward scattering whereas 1 indicates forward scattering. A value of 0 for the anisotropic factor corresponds to isotropic scattering. Mathematically, g is given by the following expression

$$g = \frac{\int_{4\pi} p(cos\theta) cos\theta d\Omega}{\int_{4\pi} p(cos\theta) d\Omega} \tag{2.5}$$

Where $p(cos\theta)$is the scattering phase function (to be discussed in the following subsection). The illustration below highlights the key events that take place in a scattering interactions.[7]

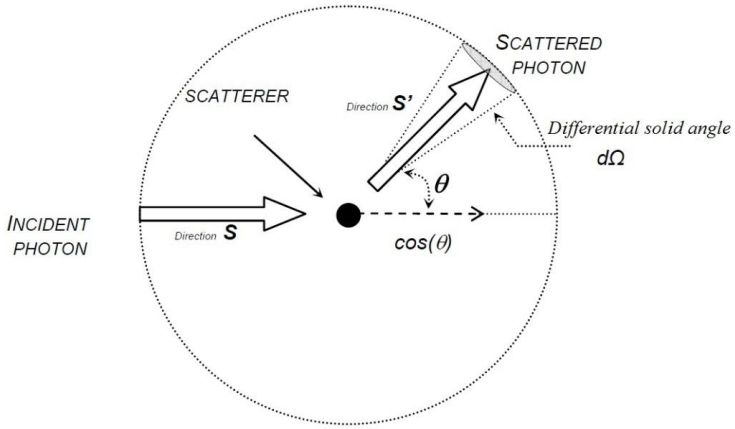

Figure 11 Elastic scattering of a photon (Mobley and Vo-Dinh 2003)

2.2.4 The scattering phase function ($p\ (\cos\theta)$)

The scattering phase function is the probability density (per unit angle) for the deflection angle, θ. From this quantity, one can obtain the probability for a photon traveling initially along $\boldsymbol{s}$ will get scattered to a direction $\boldsymbol{s'}$. There exists a variety of phase functions whose properties have been reported in the literature.[8] As an example, the Henyey-Greenstein phase function, originally proposed to describe galactic scattering, is given by

$$p(\cos\theta) = \frac{1-g^2}{2(1+g^2-2g\cos\theta)^{3/2}} \tag{2.6}$$

From g and μ_s, the effective distance (transport mean free path) traversed by a scattered photon before its direction is completely randomized can be defined as follows:

$$mfp = \frac{1}{(1-g)\mu_s} \tag{2.7}$$

The expression in the denominator is defined as the reduced scattering coefficient μ_s' a quantity that will be important later in modeling light transport. Typical values of μ_s' for biological tissues obtained in the near-infrared are listed in the Table 1.[9],[10]

Table 6 Reduced scattering coefficients of biological tissues measured at near-infrared wavelengths.

Tissue type	$\boldsymbol{\mu_s'(mm^{-1})}$	Wavelength(nm)
Skin (Caucasian)	0.241	700
Human dermis	5.60	650
Human stomach wall mucosa	4.8	700

2.3 Modeling Light Transport

The propagation of light in a turbid medium is a highly complex process. A model that fully accounts for the interaction of light with the medium's constituent particles and the nature of outgoing light is given in transport theory by the radiative transport equation (RTE). The reader is referred to the literature for a full treatment of RTE. Briefly, it is an integro-differential equation that treats light as an ensemble of localized, incoherent photons.[11] For a packet of photons traveling along a direction $\hat{\boldsymbol{s}}$, losses in intensity are attributed to absorption and scattering events that change the packet's direction of travel to some other direction $\hat{\boldsymbol{s}}$' . Gains in intensity, on the other hand, come from light that has been scattered into $\hat{\boldsymbol{s}}$.

In the near-infrared region, the interaction of light with human tissue is characterized by diffuse scattering.[12] This allows us to make use of the diffusion approximation. Briefly, the assumptions that underlie this model of light transport are the following:

(i) Scattering events are more probable than absorbing events.

(ii) All sources of scattering are isotropic.

(iii) The photon flux is constant, i.e., $\frac{d\mathbf{J}(\mathbf{r},t)}{dt} = 0$.

(iv) Phase scattering function is independent of the absolute angle and instead depends exclusively on $\hat{\mathbf{s}} \cdot \hat{\boldsymbol{s}}'$ (Figure 11).

These assumptions reduce the RTE to a more tractable model called the diffusion equation (DE). The time-dependent diffusion equation is given by

$$\frac{\partial \Psi(\mathbf{r},t)}{c\partial t} + \boldsymbol{\nabla} \cdot \mathbf{J}(\mathbf{r},t) + \mu_a \Psi(\mathbf{r},t) = q(\mathbf{r},t) \tag{2.8}$$

Where $\mathbf{J}(\mathbf{r},t) = -D(\mathbf{r})\boldsymbol{\nabla}\Psi(\mathbf{r},t)$ is the total photon current density (Fick's 1st law) and is expressed units of $\mathrm{N} \times \mathrm{L}^{-2} \times \mathrm{T}^{-1}$, where N,L and T stands for number of photons, length, and time respectively; $\Psi(\mathbf{r},t)$is a scalar quantity expressed in the same units as $\mathbf{J}(\mathbf{r},t)$ (a vector quantity); $q(\mathbf{r},t)$ is the source term expressed in units of $\mathrm{N} \times \mathrm{T}^{-1}$; c is the speed of light in the medium whose value is taken to be ~0.3mm/ps; $D(\mathbf{r})$, called the diffusion coefficient expressed, is expressed in units of L^{-1} and is given by:

$$D(\mathbf{r},t) = \frac{1}{3[\mu_a(\mathbf{r}) + \mu_s'(\mathbf{r})]} \tag{2.9}$$

Farrell and Patterson (1992) have applied the diffusion model to study the behavior of light in tissue-simulating phantoms under steady-state reflectance with the overall aim of extracting the optical properties of characterizing a turbid sample.[3] They modeled the tissue-mimicking slab to be a semi-infinite medium where a pencil beam is incident normal to the surface. After penetrating the medium, the model assumes that isotropic scattering occurs at a depth of one mean free path below the tissue-air boundary. Therefore, a pencil beam can be modeled as an isotropic point-like source located at a depth of $1/\mu_s'$. Diffusely-scattered light returning to the surface-air boundary is collected by a detecting fiber at a distance ρ from the source fiber. In their modeling technique, a mirror image is placed at a distance of $2z_b + z_o$ above the tissue-air boundary. Using this arrangement, they imposed that the photon fluence decay to zero at $z = -z_b$ (Figure 12).[13],[14] In addition, the reflectance for an extended line of isotropic scattering sources, characterized by a source strength that decreases exponentially with depth, and isotropic source were obtained for a matched and mismatched indices of refraction between the turbid media and the ambient medium (Fig. 13). Although their study examined the effects of modeling the source both as one point-like scattering site and as an extended line of scattering sites, the focus of this discussion will be confined to the results they obtained for the former as this study exclusively explores the effect of using a single isotropic scattering site albeit in a layered tissue model.

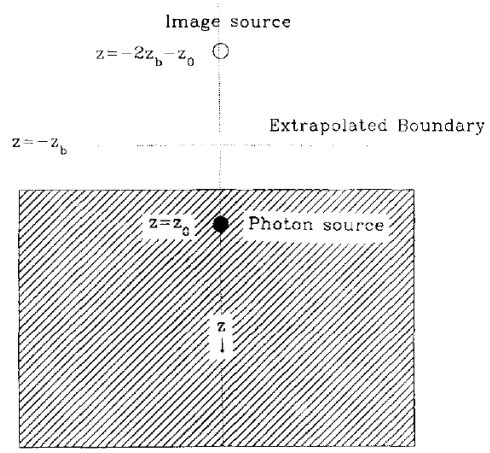

Figure 12 Incident light is scattered at a depth of one mean-free-path below the surface of the medium. Also shown is the image source employed in the extrapolated boundary condition. (Image reproduced from Ref. [3])

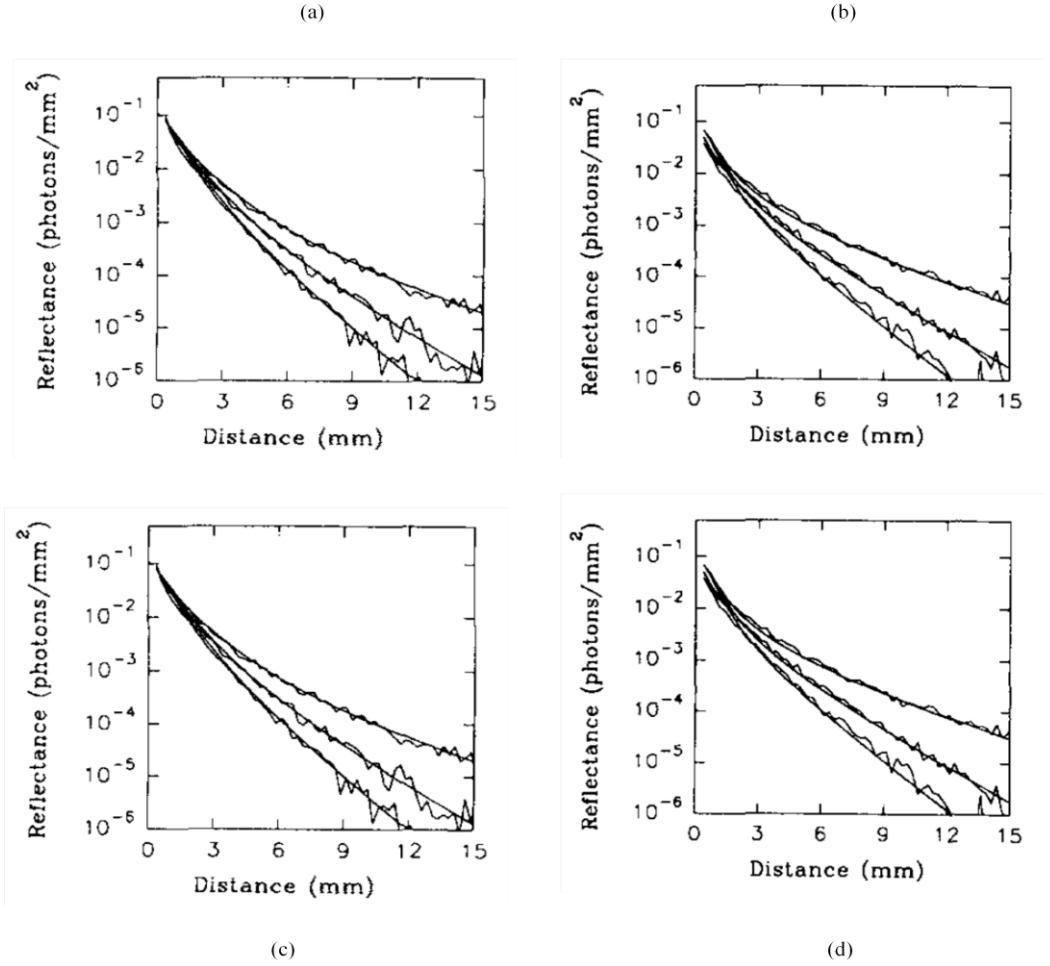

Figure 13 Reflectance from a turbid sample as calculated by Monte Carlo simulations (noisy lines) and diffusion theory (smooth lines). Single scatterer source for matched (a) and mismatched (b) indices of refraction are shown. Reflectance coming from an extended scattering source for a match (b) and mismatch in the index of refraction are also shown. (Image reproduced from Ref. [3]).

2.4 Absorption and scattering in the brain

This section is based on Refs. [15],[16] and [17].

The brain is a core component of the central nervous system that receives and relays information to and from the body. It is surrounded by a watery substance called the cerebrospinal fluid (CSF) and encased collectively by a fixture of tissues comprised of a membranous layer known as the meninges, the skull and a layer of skin (scalp). A brief description of these tissues is discussed below.

2.4.1 Skin

The skin is a barrier that protects the internal structures and organs of the body and is the largest component of the mammalian integumentary system (Fig. 14). It is mainly composed of two layers; the epidermis and the dermis.

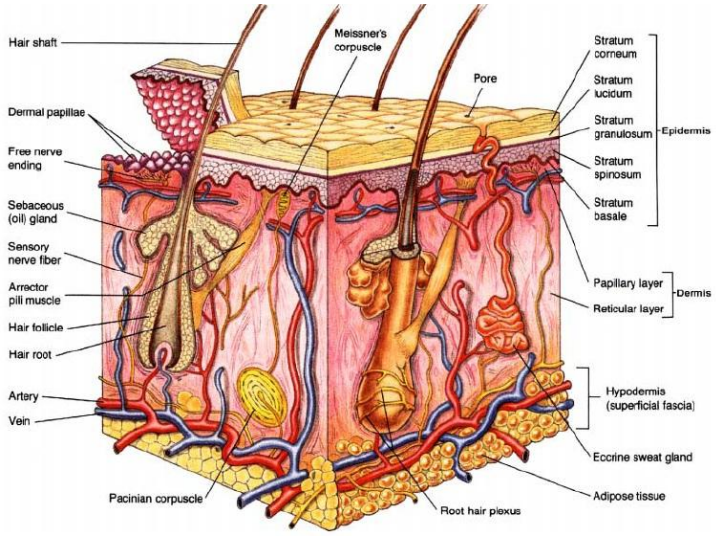

Figure 14 Anatomical cross-section of the skin. (Image reproduced from Ref. [17])

- Epidermis: is the non-vascularized region of the skin made up mainly of dead cells that are sloughed off upon replacement of new cells from underlying areas.

- Dermis: the vascularized domain of skin composed mainly of a papillary and reticular layer. It also contains the component that is responsible for the sensation of touch called mechanoreceptors
- Hypodermis: composed largely of connective tissue and adipose; anchors the skin to muscles and bones.

2.4.2 Skull

The skull is a collection of fused bone fragments that are joined together at areas called sutures (Fig 15a). The bones of the skull are grouped according to their physical appearance (long, short, flat or irregular) and are composed of two types of ossified tissue: spongy and compact. In the majority of skull bones, the spongy layer is situated between two flat compact bones (Fig 15b).

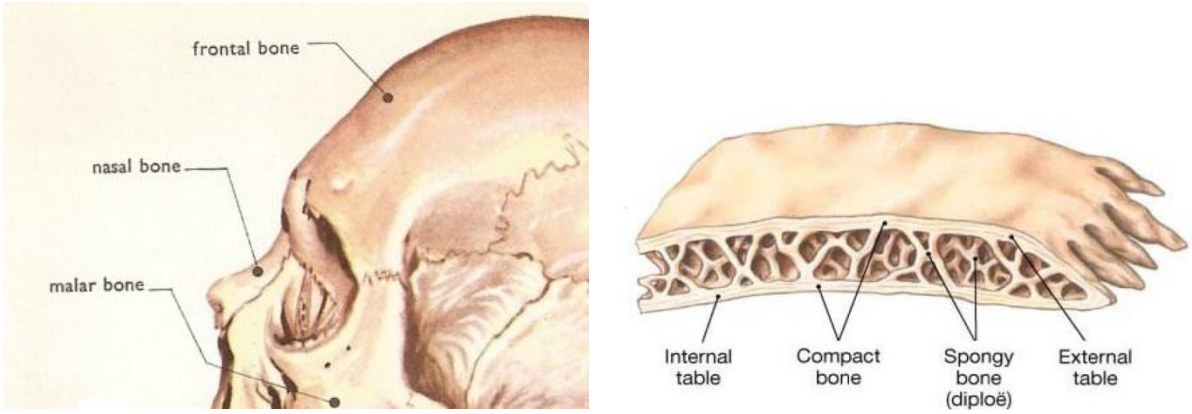

Figure 15 (a)The different bones of the skull its (b) architecture (Image reproduced from Ref. [12]).

2.4.3 Meninges

The meninges are composed of membranous connective tissue layers that enclose the cerebrospinal fluid and the brain. The outermost layer is known as the dura whereas the innermost layer is called the pia mater. Its location with respect to the structures mentioned previously is shown below.

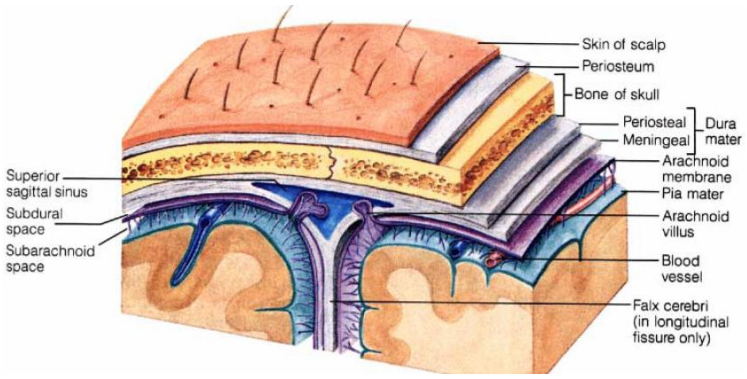

Figure 16 Meninges are composed primarily of the outer dura mater and inner pia mater {Image reproduced from Ref. [17])

2.4.4 Cerebrospinal fluid

The cerebrospinal fluid is a clear, watery substance that bathes and nourishes the brain. The optical properties of the cerebrospinal fluid has been measured by Okada *et al*. (1993).[17]

2.4.5 The brain

The brain is composed of a dense three-dimensional network of neurons that perform communicative functions by the transmission of electric signals. The two main parts of a neuron are the cell body (soma) and a slender extension that juts out from it called the axon (Fig. 17). The cerebral cortex is composed of white and grey matter. White matter owes its name to the myelin that sheaths the axons and is the medium through which signals are shuttled between axons. Grey matter, on the other hand, are composed chiefly of the soma. *Ex vivo* values of the optical properties of grey and white matter have also been reported.[19]

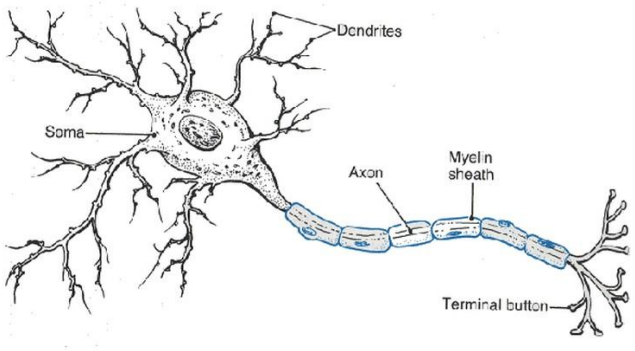

Figure 17 A neuron with a localized cell body and protruding myelinated axon. (Image reproduced from Ref. [15])

Table 7 Optical properties of grey and white matter measured at near-infrared wavelengths (A.N. Yaroslavsky *et al.* 2001)

Tissue type	$\mu_a(mm^{-1})$	$\mu_s'(mm^{-1})$	Wavelength (nm)
Grey matter	0.02	0.99	630
White matter	0.15	5.404	630

2.5 The two –layer model

Studies have been carried out previously to determine μ_a and μ_s' of tissue by solving the diffusion equation for a geometry that treats the illuminated tissue as a homogeneous, semi-infinite medium.[3] Tissues, however, are highly heterogeneous and do not always display the high degree of uniformity suggested by this model. The human head, in particular, presents a layered anatomy consisting chiefly of extra- and intra-cerebral domains. The scalp, cerebrospinal fluid (CSF) and skull comprise the former while the brain accounts for the latter.[18] Consequently, assuming a homogeneous tissue structure to extract μ_a and μ_s' will have limitations in discriminating between the contributions of tissue areas differing in these parameters to optical data. For certain organs, tissue architecture can be envisioned as a complex stack of materials layered on top of each other, each differing in its absorptive and scattering properties. As such, a refinement of the model describing its architecture is required. Models that address this high degree of non-uniformity have been proposed to reproduce the anatomical variations in tissue structure.[20] However, the lengthy computation time involved in employing such a model and

sensitivity to artifacts has been a major setback in translating this technique into a viable scheme in estimating the optical parameters.[21] Although analytical models cannot be used to describe complex distribution of a medium's optical properties, they are very fast and have been used as forward models in the inversion procedure. Kienle *et al*. explored the possibility of determining the optical properties of a heterogeneous tissue model by solving the diffusion equation for a two-layered turbid medium consisting of a superficial layer of finite depth with optical properties given by μ_{a1} and μ'_{s1} and a homogeneous, semi-infinite bottom layer characterized by μ_{a2} and μ'_{s2}.[22] The results from Kienle's work were applied to time-resolved measurements on the human forearm where diffuse reflectance was measured at a source-detector separation of 16.3mm and 20.3mm for a superficial layer thickness of 5mm.[23]

The tissue of interest in this investigation will be that of the head with the goal of determining μ_a and μ'_s of the brain. For this purpose, Monte Carlo data representative of the infant and adult head were generated In this study, the head is envisioned as a two-layered system; the bottom layer is taken to be a homogeneous, semi-infinite region representing the brain whereas the superficial layer is of finite thickness and accounts for all the overlying structures. A schematic of the system is given below.

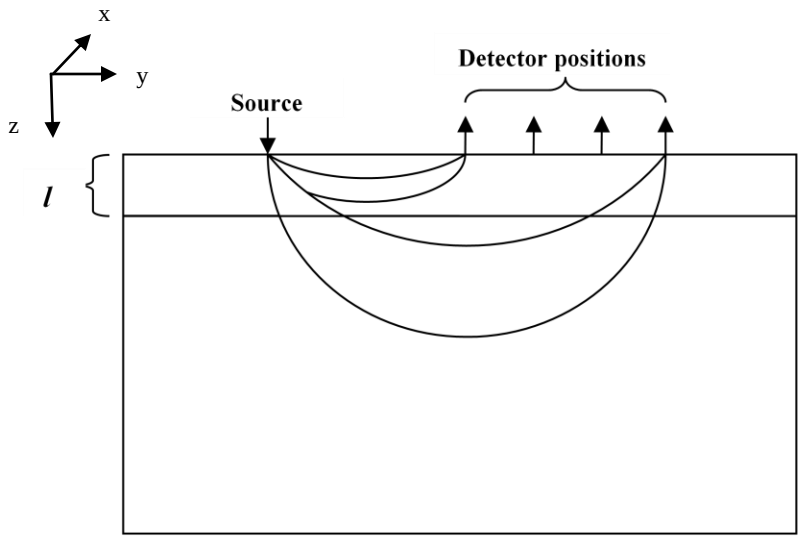

Figure 18 Two-layer model of the brain. The top layer is of finite thickness *l*(mm) ad the bottom layer is treated as a semi-infinite homogeneous medium. A reference coordinate system is also shown.

In the configuration above, an infinitely thin pencil beam is incident at $z = 0$ after which it is isotropically scattered at a depth of $z = z_o = \frac{1}{\mu'_{s1}}$ which in this study is located in the superficial layer. The (x,y) coordinate system is located on the surface of the medium. In the frequency domain, the diffusion equation for the two-layered system is described by:

$$D_1\nabla^2\,\Psi_1(\mathbf{r}) - \,(\mu_{a1} + \tfrac{i\omega}{c})\Psi_1(\boldsymbol{r}) = \,-\delta(x,y,z-z_o) \qquad 0 \le z < l \qquad (2.10)$$

$$D_2\nabla^2\,\Psi_2(\mathbf{r}) - \,(\mu_{a2} + \tfrac{i\omega}{c})\Psi_2(\boldsymbol{r}) = \,0 \qquad l \le z \qquad (2.11)$$

The approach taken in this work for solving the pair of equations above is similar to that employed by Kienle. First, the equations are converted to ordinary differential equations (ODE) by making use of the 2D Transverse Fourier transform, i.e., only the transverse coordinates *x* and *y* are transformed.

$$\varphi_k(z,s_1,s_2) = \iint_{-\infty}^{\infty}\Psi_k(x,y,z)e^{i(s_1x+s_2y)}dxdy \qquad (2.12)$$

where Ψ_k is the AC component denoting the solution in the k^{th} layer (k = 1,2).

Eqs. (2.10) and (2.11) then become

$$\frac{\partial^2\varphi_1(z,s)}{\partial z^2} - \alpha_1^2\varphi_1(z,s) = -\frac{\delta(z-z_o)}{D_1} \qquad 0 \le z < l \quad (2.13)$$

$$\frac{\partial^2\varphi_2(z,s)}{\partial z^2} - \alpha_2^2\varphi_2(z,s) = 0 \qquad l \le z \quad (2.14)$$

Since this study aims to recover the values of the two-layered system using the multi-distance method in the frequency domain, α_k in Eqs. (2.13) and (2.14) are given by $\alpha_k = \sqrt{\frac{D_k s^2 + \mu_{ak} + i\frac{\omega}{c}}{D_k}}$, $s^2 = s_1^2 + s_2^2$ where s_1 and s_2 are coordinates in the inverse Fourier space in units of L^{-1} (inverse length). Eqs. (2.13) and (2.14) were solved by applying the four boundary conditions listed below:

$$\varphi_1(-z_b, s) = 0 \quad (2.15)$$

$$\varphi_2(\infty, s) = 0 \quad (2.16)$$

$$\frac{\varphi_1(l,s)}{\varphi_2(l,s)} = \frac{n_1^2}{n_2^2} = 1 \quad (2.17)$$

$$D_1\frac{\partial\varphi_1(z,s)}{\partial z}\Big|_{z=l} = D_2\frac{\partial\varphi_2(z,s)}{\partial z}\Big|_{z=l} \quad (2.18)$$

It should be noted that Eq (2.13) implies a discontinuity in $\frac{\partial\varphi_1}{\partial z}$ which should be considered in solving the system. The extrapolated boundary condition (EBC) was used in (2.16) for the tissue-air interface. Briefly, it states that the fluence decays to zero at a distance z_b beyond the surface.[13],[14] It is given by:

$$z_b = \frac{1+R_{eff}}{1-R_{eff}}2D_1 \quad (2.19)$$

R_{eff} gives the amount of photons that is diffusely reflected at the air-tissue boundary[3] whose value in Eq. (2.19) is given by 0.493 for a refractive index mismatch of 1.4 between the turbid and ambient medium.

The solutions of (2.13) and (2.14) are:

$$\varphi_1(z,s) = \frac{\sinh[\alpha_1(z_b+z_o)]}{D_1\alpha_1}\left\{\frac{D_1\alpha_1\cosh[\alpha_1(l-z)]+D_2\alpha_2\sinh[\alpha_1(l-z)]}{D_1\alpha_1\cosh[\alpha_1(l+z_b)]+D_2\alpha_2\sinh[\alpha_1(l+z_b)]}\right\} - \frac{\sinh[\alpha_1(z_o-z)]}{D_1\alpha_1}, \quad 0 \le z < z_o \quad (2.20)$$

$$\varphi_1(z,s) = \frac{\sinh[\alpha_1(z_b+z_o)]}{D_1\alpha_1}\left\{\frac{D_1\alpha_1\cosh[\alpha_1(l-z)]+D_2\alpha_2\sinh[\alpha_1(l-z)]}{D_1\alpha_1\cosh[\alpha_1(l+z_b)]+D_2\alpha_2\sinh[\alpha_1(l+z_b)]}\right\}, \qquad z_o < z < l \qquad (2.21)$$

$$\varphi_2(z,s) = \frac{\sinh[\alpha_1(z_b+z_o)]e^{\alpha_2(l-z)}}{D_1 1\alpha_1\cosh[\alpha_1(l+z_b)]+D_2\alpha_2\sinh[\alpha_1(l+z_b)]}, \qquad l \le z \qquad (2.22)$$

These results are then converted back to Ψ_k by performing a 2D inverse Fourier transform:

$$\Psi_k = \frac{1}{(2\pi)^2}\iint_{-\infty}^{\infty}\varphi_k(z,s)e^{-i(s_1x+s_2y)}ds_1ds_2$$

$$= \frac{1}{2\pi}\int_0^{\infty}\varphi_k(z,s)sJ_0(s\rho)ds \qquad (2.23)$$

Where ρ is the source-detector separation and J_0 is the zeroth-order Bessel function of the first kind. A full derivation of Eqs. (2.13) - (2.14) and Eqs. (2.20) - (2.22) are given in Appendix A.

The spatially-resolved reflectance is given by Fick's law:

$$R(\rho) = D_1\frac{\partial\Psi_1(\rho,z)}{\partial z}\Big|_{z=0} \qquad (2.24)$$

where the z-axis originates at the source location and points downward into the medium (Figure 18).

The amplitude (AC) of the intensity of the sinusoidally-modulated light (f = 110MHz) and the phase delay respectively are given by

$$AC = \sqrt{Im[R(\rho,\omega)]^2 + Re[R(\rho,\omega)]^2} \qquad (2.25)$$

$$\theta = \tan^{-1}\frac{Im[R(\rho,\omega)]}{Re[R(\rho,\omega)]} \qquad (2.26)$$

Chapter 2 References

[1] R. Serway and J. Jewett, *Physics for Scientists and Engineers* (Brooks Cole, Belmont, California, 2010). Chapter 1

[2] F.L. Pedrotti, L.M. Pedrotti and L.S. Pedrotti, *Introduction to Optics* ( )

[3] T.J. Farrell, M.S. Patterson, and B. Wilson, "A diffusion theory model of spatially resolved, steady-state diffuse reflectance for the noninvasive determination of tissue optical properties *in vivo*," Med. Phys. **19**(4), 879-888, (1992).

[4] S.R. Arridge, M. Schweiger, M. Hiraoka, and D.T. Delpy, "A finite element approach for modeling photon transport in tissue," Med. Phys. **220**, 299-309 (1993).

[5] J. Mobley and T. Vo-Dinh, "Optical Properties of Tissue,"in *Biomedical Photonics Handbook,* T. Vo-Dinh, Editor (CRC Press, 2003) pp. 1-10

[6] G. Zaccanti, S. Del Bianco, F. Martelli, "Measurements of optical properties of high-density media," Appl. Opt. **42**, 4023 (2003)

[7] A. Ishimaru, *Wave Propagation and Scattering in Random Media* (Academic, New York, 1997).

[8] A. Kienle, F.K. Forster, and R. Hibst, "Influence of the phase function on determination of the optical properties of biological tissue by spatially resolved reflectance," Optics Letters **26**, 1571-1573 (2001).

[9] W. Cheong, S.A. Prahl, and A.J. Welch, "A review of the optical properties of biological tissues," IEEE Journal of Quantum Electronics **26**, 2166-2185 (1990).

[10] A. Bashkatov, E. Genina, V. Tuchin, "Tissue Optical Properties," in *Handbook of Biomedical Optics*, David, C, Pitris, and N. Ramanujam, Editors (CRC Press,2011), pp.67-100

[11] A. Sassaroli, *Fundamental studies of near Infrared spectroscopy and diffuse optical tomography for biomedical diagnosis.* PhD thesis, University of Electro-Communication in Tokyo, Japan, 2002

[12] G. Branco, *The development and evaluation of head probes for optical imaging of the infant head* PhD Thesis, University College London, January 2007. Chapter 2

[13] S. Fantini S, MA Franceschini, and E. Gratton, " Semi-infinite-geometry boundary problem for light migration in highly scattering media: a frequency-domain study in the diffusion approximation," J Opt Soc Am **11**:2128–2138 (1994)

[14] A. Kienle and M.S. Patterson, "Improved solutions of the steady-state and the time-resolved diffusion equations for reflectance from a semi-infinite turbid medium," J. Opt. Soc. Am. **14**, 246-254 (1997)

[15] A. Vander, J. Sherman, and D. Luciano, *Human Physiology: The Mechanisms of Body Functions* (McGraw-Hill, NY,2004)

[16] A.N. Carlson, Niel. A. *Foundations of Physiological Psychology*. (Needham Heights, Massachusetts, 1992)

[17] *Online resource*: Human brain physiology pdf (no author)

[18] E. Okada, M. Firbank and D.T. Delpy, "The effect of overlying tissue on the spatial sensitivity profile of near-infrared spectroscopy," Phys. Med. Biol. **40**, 2093-2108 (1995)

[19] A.N. Yaroslavsky, P.C. Schulze, I.V. Yaroslavsky, R. Schober, F. Ulrich, and H.J. Scwarzmaier, "Optical properties of selected native and coagulated human brain tissues in vitro in the visible and near infrared spectral range," Phys. Med. Biol. **47**, 2059-2073 (2002).

[20] E. Okada, M. Firbank, M. Schweiger, S.R. Arridge, M. Cope and D.T. Delpy, "Theoretical and experimental investigation of near-infrared light propagation in a model of the adult head," Appl. Opt **36**, 21-31 (1997)

[21] F. Fabbri, A. Sassaroli, M.E. Henry and S. Fantini, "Optical measurements of absorption changes in two-layered diffusive media," Phys. Med. Biol. **49**, 1183-1201 (2004).

[22] A. Kienle, T. Glanzmann, M.S. Patterson, N. Utke, R. Bays, G. Wagniéres, and H. van der Bergh, "Noninvasive determination of the optical properties of two-layered turbid media," Appl. Opt. **37**, 779-791 (1998)

[23] A. Kienle and T. Glanzmann, "In vivo determination of the optical properties of muscle with time-resolved reflectance using a layered model," Phys. Med. Biol **44**, 2689-2702 (1999).

[24] M.L. Boas, Mathematical Methods in the Physical Sciences (John Wiley & Sons, Hoboken, New Jersey, 1983)

Chapter 3: Determination of the Optical Properties of a Two-layered Medium as a Model of the Head

3.1 The Monte Carlo Approach

The depiction of light as discrete bundles of photons undergoing random collisions allows us to investigate the statistical aspects of light propagation in a diffusive medium. Upon injection, a photon follows a convoluted path due to multiple scattering events. In a semi-infinite medium, the photon exits the medium through the same plane where it was injected and the volume probed by the detected light is confined in a banana-shaped region where individual photon paths are interspersed with each other.

Monte Carlo methods rely on several independent samplings of a variable that correspond to the quantity of interest. The "true" value of this quantity is then obtained by taking the average value of this random variable.[1] These variables inherit their arbitrary character by being defined in terms of a randomly-generated number ξ between 0 and 1.[2],[3] The probability density function (PDF) $p(\chi)$ for a random variable χ defined over the interval $(-\infty, \infty)$ allow us to determine its value from ξ. Mathematically,

$$\int_{-\infty}^{A} p(\chi) d\chi = \xi. \tag{3.1}$$

The Monte Carlo method is a powerful tool that is widely used in modeling the probabilistic nature of light-tissue interaction. Along with their respective PDFs, variables that specify the "history" of the detected photon – pathlength, deflection angle and azimuthal angle – can be used to extract their expectation value after being sampled repeatedly. For instance, since the photon can either be scattered or absorbed in a diffusive medium, the PDF of the photon pathlength can be obtained from the interaction coefficient (μ_t). It is defined as the sum of the absorption and scattering coefficients, $\mu_t = \mu_a + \mu_s$ and stands for the probability of photon interaction per unit infinitesimal pathlength confined in an interval (r,r+dr).[3] From this description, the following formulation is made:

$$\mu_t = \frac{-dP\{r+dr \geq r' \geq r\}}{P\{r' \geq r\}dr} \tag{3.2}$$

A solution for *P* can be obtained by integrating it in the range (0,*l'*)

$$P\{r' \geq l'\} = e^{-\mu_t l'} \tag{3.3}$$

The equation above stands for the probability of a photon's survival after traversing a distance *l'*.

Before proceeding to define the PDF, we recall the definition of the cumulative probability function (CDF), $P(Z)$.[4] For a random variable χ defined in $(-\infty, \infty)$ with a PDF of $p(\chi)$, the CDF is given by:

$$P(Z) = \int_{-\infty}^{Z} p(\chi) d\chi \tag{3.4}$$

Re-ordering of Eq. (3.3) gives the CDF of *r'*, which stands for the probability of a photon to become extinct in the interval (0,*l'*):

$$P\{r' < l'\} = 1 - e^{-\mu_t l'} \tag{3.5}$$

In the Monte Carlo simulation, a random number ξ_1 uniformly distributed in (0,1) is generated and assigned to this probability,

$$\xi_1 = 1 - e^{-\mu_t l} \xrightarrow{solving\ for\ l} l = -\frac{1}{\mu_t}\ln(1-\xi_1) \tag{3.6}$$

Eq. (3.6) gives us *l* in terms of ξ_1. To determine how their respective PDFs are related, we invoke the definition of the PDF of a set of transformed variables. For instance, if $y = f(x)$ then p_y (PDF of *y*) is related to p_x (PDF of *x*) through $p_y dy = p_x dx$. This follows from the fact that the probability in an infinitesimal area should not change by a transformation of variables.[5] The PDF of *l* can then be obtained as follows:

$$p_l = p_{\xi_1} \frac{d\xi_1}{dl} = p_{\xi_1}\left(\mu_t e^{-\mu_t l}\right) \tag{3.7}$$

Since ξ_1 is uniform in (0,1), p_{ξ_1}=1. Thus, the PDF of the pathlength is given by:

$$p_l = \mu_t e^{-\mu_t l} \tag{3.8}$$

The PDF of ϕ, assuming that it is uniformly distributed over (0,2π), is given by $p(\phi) = \frac{1}{2\pi}$. For a random number ξ_2 assigned to the CDF of ϕ', and by virtue of Eq. (3.4),

$$\xi_2 = \int_0^{\phi} p(\phi')d\phi' = \frac{\phi}{2\pi} \xrightarrow{solving\ for\ \phi} \phi = 2\pi\xi_2 \tag{3.9}$$

As for the PDF of θ, the Henyey-Greenstein phase function is used for biological tissues,

$$p(\cos\theta) = \frac{1-g^2}{2(1+g^2-2g\cos\theta)^{3/2}} \tag{3.10}$$

Where g is the anisotropic factor discussed in subsection 2.2.3. For a random number ξ_3, Eq (3.4) is again used to obtain θ,

$$\xi_3 = 2\pi \int_0^{\theta} p(\cos\theta')\sin\theta' d\theta' \xrightarrow{solving\ for\ \cos\theta} \cos\theta = \begin{cases} 2\xi_3 - 1\ if\ g = 0\ (\text{isotropic scattering}) \\ \frac{1}{2g}\{1 + g^2 - \left[\frac{1-g^2}{1-g+2g\xi_3}\right]^2\}\ if\ g \neq 0 \end{cases} \tag{3.11}$$

In this study, isotropic scattering is assumed between successive changes in direction of photon propagation.

For a refractive index mismatch between the diffusive and ambient medium, an additional step is necessary to decide whether the photon is reflected or transmitted.[2],[3] A fourth random number ξ_4 can be generated and compared with the reflection coefficient for unpolarized light,

$$R_{tot} = \frac{R_{par}+R_{per}}{2} \tag{3.12}$$

If $R_{tot} > \xi_4$, the photon is reflected and if $R_{tot} < \xi_4$ then the photon is transmitted.

R_{par} and R_{per} are given by:

$$R_{par} = \left(\frac{tg(\theta_i - \theta_t)}{tg(\theta_i + \theta_t)}\right)^2 \tag{3.13}$$

$$R_{per} = \left(\frac{\sin(\theta_t - \theta_i)}{tg(\theta_i + \theta_t)}\right)^2 \tag{3.14}$$

It should be noted that $(\xi_1, \xi_2, \xi_3, \xi_4)$ are uniformly distributed in (0,1) in all of the cases above.

In this study, each of the N_o injected photons is traced until they are either detected or lost through the boundaries of the two-layer medium. These simulations are performed in the time domain (TD) and the detected photons are then grouped according to the time spent in the medium prior to detection. A single simulation performs these tracings over a pre-defined set of source-detector distances. A time interval, say (0,T), over which the outgoing photon flux are detected are then divided into N_T subintervals, all having equal width Δt_k centered at a particular time t_k. For a pencil beam input where the source is given by a Dirac delta $\delta(t)$, $S(\boldsymbol{r}, \hat{\boldsymbol{s}}, t) = N_o \delta(\boldsymbol{r}) \delta(\hat{\boldsymbol{s}} - \widehat{s'}) \delta(t)$, the intensity of detected photons arriving at different times form an intensity profile that is broadened in comparison to the incident Dirac input.[7] This intensity profile is called the temporal point spread function (TPSF) and is given by[2]:

$$\text{TPSF}(t_k) = \frac{\sum_{j=1}^{m_k} e^{-\mu_{a1} l_{1_j} - \mu_{a2} l_{2_j}}}{N_o \Delta S \Delta t}. \tag{3.15}$$

The Fourier transform of the TPSF yields the frequency domain (FD) reflectance[8]:

$$R(\omega) = \frac{\sum_{k=1}^{N_T} (\sum_{j=1}^{m_k} e^{-\mu_{a1} l_{1_j} - \mu_{a2} l_{2_j}}) e^{-i\omega t_k}}{N_o \Delta S}, \omega = 2\pi f \text{ where } f = 110\text{MHz} \tag{3.16}$$

Where:

j: an index that denotes the number of photons

N_o: total number of injected photons

$l_{1_j}(mm)$: Photon pathlength in layer 1

$l_{2_j}(mm)$: Photon pathlength in layer 2

$\mu_{a1}(mm^{-1})$: Absorption coefficient of layer 1

$\mu_{a2}\ (mm^{-1})$: Absorption coefficient of layer 2

$\Delta S(mm^{-2})$: Area of detector Δt(ns): Time interval

m_k: Number of photons in a subinterval centered at t_k N_T: number of subintervals

k: an index that denotes the k^{th} subinterval

In our simulation, a total of 300 time subintervals and 10,000 injected photons were used.

Lastly, the AC and phase are then obtained from $R(\omega)$ as follows:

$$AC(mm^{-2}) = \|R(\omega)\|. \quad (3.17)$$

$$\theta = \text{Arg}(R(\omega)). \quad (3.18)$$

3.2 Forward Modeling

Monte Carlo data simulating light propagation in a two-layer turbid medium were generated for a case representative of infant and adult foreheads. These are characterized by a superficial layer thickness of 5mm and 10mm respectively. In these simulations, the values of AC and phase – obtained from using Eq. (3.17) and Eq. (3.18) – were simulated at source-detector separations ranging from 5mm to 60mm in the frequency domain. The same pair of quantities was compared with those obtained from solving the diffusion equation for a two-layered system.

Due to numerical errors encountered in performing the integration in Eq. (2.23) using Eq. (2.20) as the sole component in the integrand – which causes an erratic behavior of the AC and phase at large source-detector separations – an expansion of the hyperbolic functions in $\varphi_1(z = 0)$ in terms of its exponentials is carried out and incorporated in the evaluation of the integral (See Appendix B). This is called the limiting equation and has been employed in studies on the human forearm.[9] This hybrid model splits the integral into two parts, each being evaluated over different ranges of the integrating variable; the first makes use of Eq. (2.20) for s 0-10mm^{-1} whereas the second part employs (3.19) for values of *s* spanning 10-22mm^{1}.

$$\varphi_1^{(LE)}(z,s) = \frac{1}{2D_1\alpha_1}\left\{\left(e^{\alpha_1(z_b+z_o)} - e^{-\alpha_1(z_b+z_0)}\right)\left[\frac{(D_1\alpha_1+D_2\alpha_2)e^{\alpha_1(l-z)}+(D_1\alpha_1-D_2\alpha_2)e^{-\alpha_1(l-z)}}{(D_1\alpha_1+D_2\alpha_2)e^{\alpha_1(l+z_b)}+(D_1\alpha_1-D_2\alpha_2)e^{-\alpha_1(l+z_b)}}\right] + e^{-\alpha_1(z_o-z)} - e^{\alpha_1(z_0-z)}\right\} \quad (3.19)$$

For the first layer, Eq.(2.23) then becomes

$$\Psi_1(\rho,z) = \frac{1}{2\pi}\left\{\int_0^{10}\varphi_1(z,s)sJ_0(s\rho)ds + \int_{10}^{22}\varphi_1^{(LE)}(z,s)sJ_0(s\rho)ds\right\} \quad (3.20)$$

The integral is carried out using Gaussian quadrature in MATLAB. As shown in Fig. 19 and Fig. 20, the theoretical values of AC and phase show good agreement with simulated data, yielding a maximum error of 7%(9%) for AC and discrepancy in phase of 1.89°(1.33°) for l=5mm(10mm).

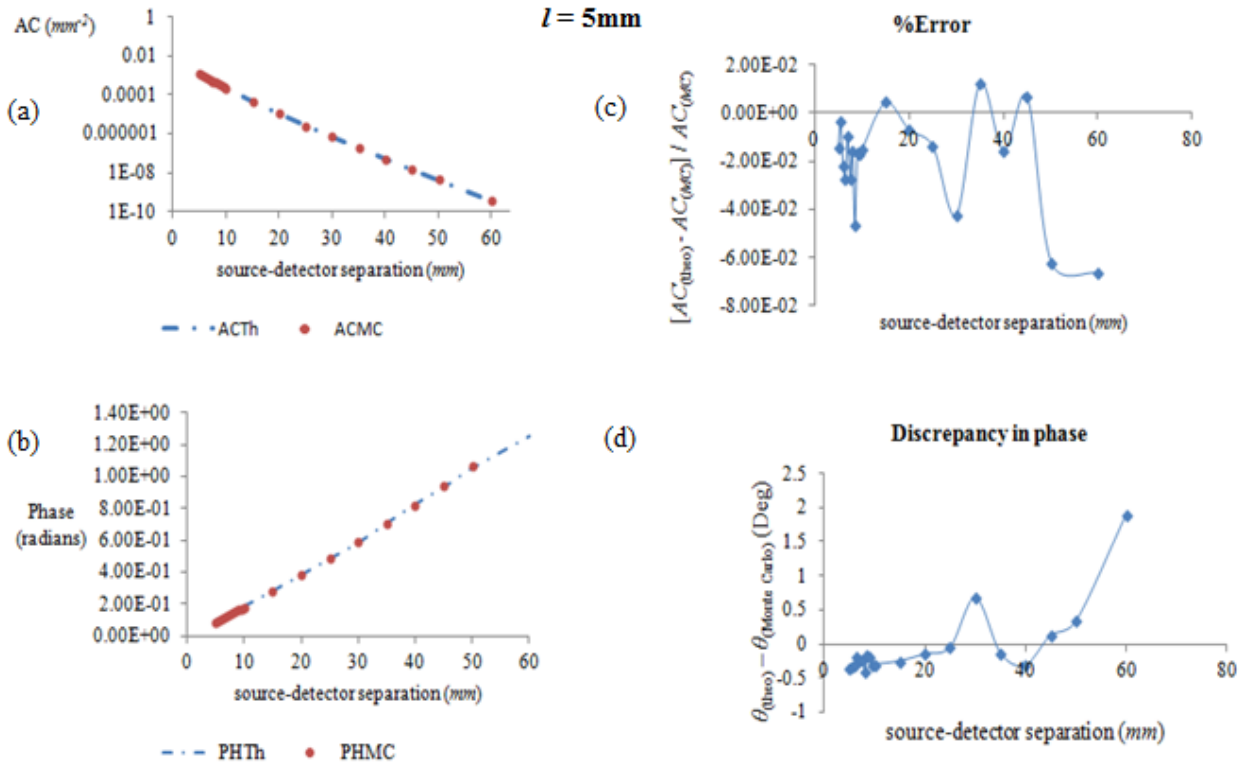

Figure 19 Comparison between simulated (filled circles) and theoretical values (dashed line) of AC and phase with accompanying measures of error for a top layer thickness of 5mm [(a)-(d)]. Monte Carlo simulations were made for a two layer system with the following optical properties: $\mu_{a1} = 0.015mm^{-1}, \mu_{s1}^{'} = 0.80mm^{-1}, \mu_{a2} = 0.01mm^{-1}, \mu_{s2}^{'} = 1.2mm^{-1}$

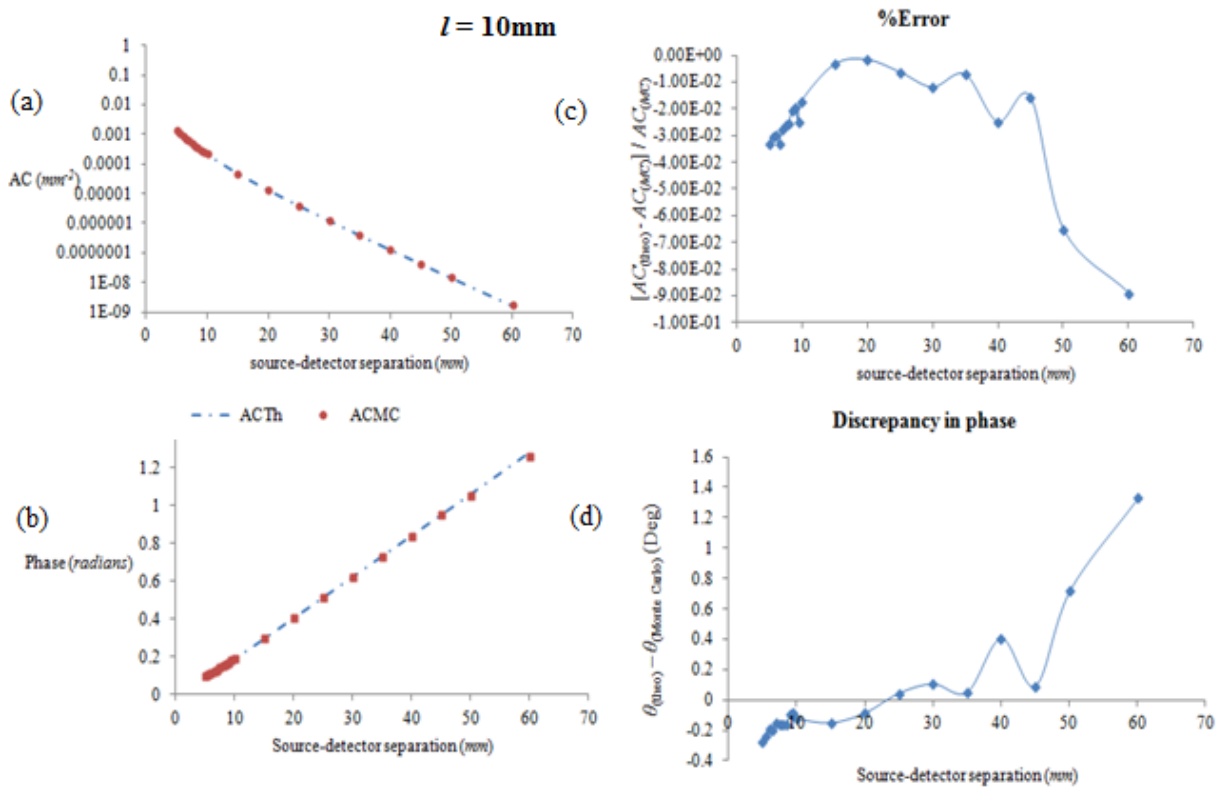

Figure 20 Comparison between simulated (filled circles) and theoretical values (dashed line) of AC and phase with accompanying measures of error for a top layer thickness of 10mm [(a)-(d)]. Monte Carlo simulations were made for a two layer system with the following optical properties: $\mu_{a1} = 0.015mm^{-1}, \mu_{s1}^{'} = 0.80mm^{-1}, \mu_{a2} = 0.01mm^{-1}, \mu_{s2}^{'} = 1.2mm^{-1}$

A layered model of tissue is also relevant in other respects. Since the intensity profile of diffusely scattered light emanating from a highly scattering medium such as biological tissue is attributable to its optical properties, the inherent heterogeneity in μ_a and μ_s' of tissues can therefore be suggestive of its architecture as the incident light probes increasing depths and encounters regions varying in these parameters. It is therefore reasonable to expect a qualitative difference in the intensity profile of reflected light between a homogeneous and layered model of tissue.

Ankri *et al.* observed that an elbow region is characteristic of intensity profiles collected for layered media by noting its absence from those of phantoms uniform in both its scattering and absorbing properties.[10] Specifically, they compared the intensity profile of reflected light from three phantoms; one two-layered phantom and two homogenous phantoms. The homogeneous phantoms possessed scattering and absorbing properties similar to each of the layers in the two-layer system. The intensity profile of the

reflected light from the two homogeneous phantoms presented a monotonic decay whereas that of from the two-layered medium followed a decay behavior similar to the homogeneous phantom with optical properties equal to the first layer's for source-detector separations within a certain range. Outside of this range, the decay profile switched to that of the homogeneous phantom with optical properties identical to that of the second layer. In the same study, they also investigated the effect of the depth of the superficial layer on the intensity profiles from the three phantoms described. They found that the transition point in the decay profile of the two-layered system appeared for smaller values of the source-detector separations for thin superficial layers whereas it became noticeable at large source-detector distances for larger values of the first layer thickness. This lends further credence to the claim that the multi-distance method becomes sensitive to deeper structures at larger source-detector separations. Furthermore, the results obtained in Figure 21 strongly corroborate the evidence for the existence of this transition point and exhibits the associated behavior in its intensity profile with respect to the thickness of the first layer.

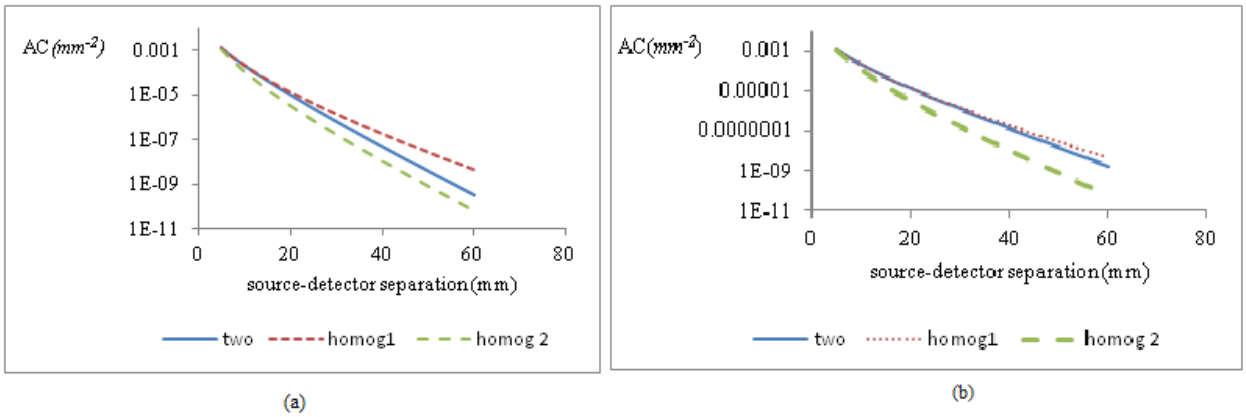

Figure 21 Reflectance profile generated from a two-layer medium using the solutions to the two-layer model (solid line) with the following optical properties: $\boldsymbol{\mu_{a1} = 0.0082mm^{-1}, \mu'_{s1} = 0.8mm^{-1}, \mu_{a2} = 0.0125mm^{-1}, \mu'_{s2} = 1.2mm^{-1}}$ for (a) $\boldsymbol{l = 5mm}$ and (b) $\boldsymbol{l = 10mm}$. The reflectance profile of a homogeneous medium with the optical properties of the top layer (round-dotted curve) and that of the bottom layer's (dashed curve) are also shown for each.

3.2 Nonlinear Inversion

The tissue of interest in this investigation will be that of the human head with the goal of determining μ_a and μ'_s of the brain. Monte Carlo data representative of the infant and adult head were generated. The two-layer model proposed by Kienle is used to retrieve μ_a and μ'_s of the two layers in the frequency

domain using the multi-distance method in reflectance geometry.[11] In this model, the brain is taken to be a semi-infinite, homogeneous medium situated underneath an extra-cerebral layer composed of the skull-scalp region. The optical properties of the bottom layer (brain) are extracted in a piecewise manner:

(i) The solution of the diffusion equation for a homogeneous model is used to determine μ_{a1} and μ'_{s1} by nonlinear regression to AC and phase at short source-detector separations (5mm–10mm in steps of 0.5mm).

(ii) μ_{a2} and μ'_{s2} are recovered by performing nonlinear regression to these Monte Carlo simulations using the solutions of the diffusion equation offered by the two-layer model at source-detector distances 5mm-60mm. In this step, the estimated parameters for the first layer, together with a known value of its thickness are used as input to the two-layer forward model. A secant version of the Levenberg-Marquardt algorithm is employed to recover μ_{a2} and μ'_{s2} in this step.

Nonlinear regression to Monte Carlo data using the solution of the diffusion equation for a two-layered system were performed using the Levenberg-Marquardt algorithm to retrieve μ_a and μ'_s for the two layers for the two cases representative of infant (l=5mm) and adult (l=10mm) foreheads. The value of the optical parameters characterizing the two layers employed in the Monte Carlo simulations can be retrieved by the following approach: knowing the set of possible values spanned by μ_a and μ'_s for a specific tissue type provide a means of narrowing down a plausible value for the initial guess, a value which is iteratively refined until a desired solution is found. A solution minimizes χ^2, defined as the sum of the squared residuals:

$$\chi^2(\mu_{ai}, \mu_{s_i'}) = \frac{1}{2}\sum_{n=1}^{k}\left\{\left(\frac{AC_{MC}-AC_{Theo}(\mu_{ai},\mu_{s_i'})}{\sigma_n^{AC}}\right)^2 + \left(\frac{\theta_{MC}-\theta_{Theo}(\mu_{ai},\mu_{s_i'})}{\sigma_n^{\theta}}\right)^2\right\} \quad (3.21)$$

Four sets of optical properties characterizing both layers were used in generating these simulated measurements. These are summarized in Table 3:

Table 3 Four sets of optical properties for a two-layer medium with a superficial layer thickness of 5mm and 10mm

Case	$\boldsymbol{\mu_{a1}(mm^{-1})}$	$\boldsymbol{\mu'_{s1}(mm^{-1})}$	$\boldsymbol{\mu_{a2}(mm^{-1})}$	$\boldsymbol{\mu'_{s2}(mm^{-1})}$
1	0.0067	0.80	0.0095	1.2
2	0.0082	0.80	0.0125	1.2
3	0.011	0.80	0.018	1.2
4	0.015	0.80	0.010	1.2

For all the results reported in the section that follows, the recovery procedure was performed with the thickness of the first layer known *a priori*. The errors for the values of the estimated parameters are displayed together with a plot comparing the recovered values with the true ones. The errors are defined as:

$$\%Error = \frac{\mu^{xi}_{(est)} - \mu^{xi}_{(true)}}{\mu^{xi}_{(true)}} \tag{3.22}$$

Where $\mu^{xi}_{(est)}$ and $\mu^{xi}_{(true)}$ correspond to the estimated and true optical coefficient – $\mu_a$or μ'_s – in the i^{th} layer respectively. The following diagram summarizes the steps involved in the recovery of the bottom layer's optical properties:

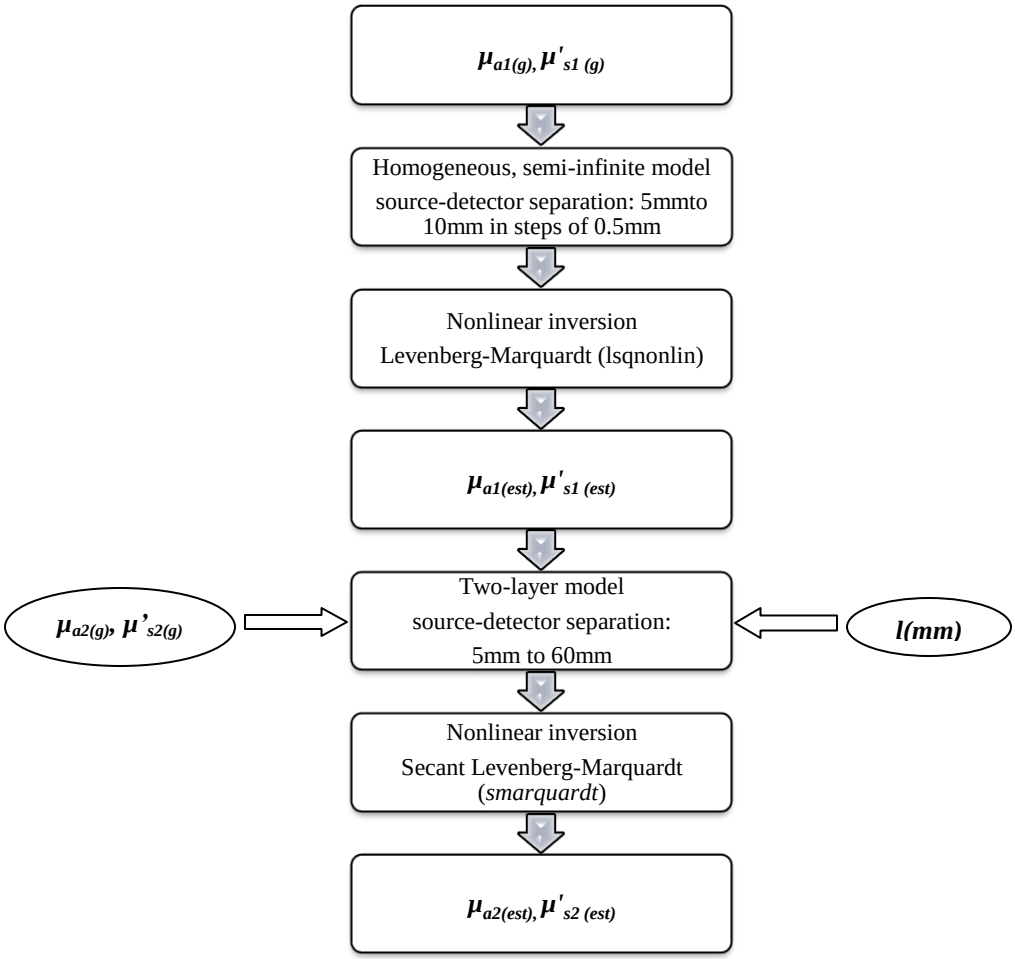

Figure 22 Steps in recovering the optical properties of the bottom layer (brain). $\mu_{ai(g)}$ and $\mu'_{si(g)}$ correspond to the initial guess for the absorption and reduced scattering coefficient for the i^{th} layer. $\mu_{ai(est)}$ and $\mu_{s'i(est)}$ are the estimated value of the optical properties for the i^{th} layer. *l* is the thickness of the first layer that is assumed to be known *a priori*.

3.3 Results

3.3.1 Recovering μ_{a1} and μ'_{s1}

For the four cases in Table 3, values of AC and phase were generated with 0.5mm increments in going from 5mm to 10mm to allow for measurements at small source-detector distances, thus rendering the recovery procedure sensitive to the optical properties of the first layer. This approach is motivated by the fact that the depth probed by diffusively scattered light depends strongly on the source-detector separation; the volume of tissue investigated by the banana-shaped bundle gains sensitivity to deeper regions at increasing source-detector

separations. Specifically, the penetration depth of the incident light is about one-fourth the source-detector distance.[12] Thus, confining the tissue volume traversed by the diffuse light within shallow depths allows us to extract the absorption and reduced scattering coefficients of the first layer. In this recovery procedure, the solution to the diffusion equation for a semi-infinite, homogeneous model was employed in obtaining μ_{a1} and μ'_{s1} by performing nonlinear regression to Monte Carlo simulated measurements using a built-in Levenberg-Marquardt algorithm in MATLAB, *lsqnonlin*. The estimates for μ_{a1} and μ'_{s1} for the two cases – infant and adult head – treated in this study are shown below.

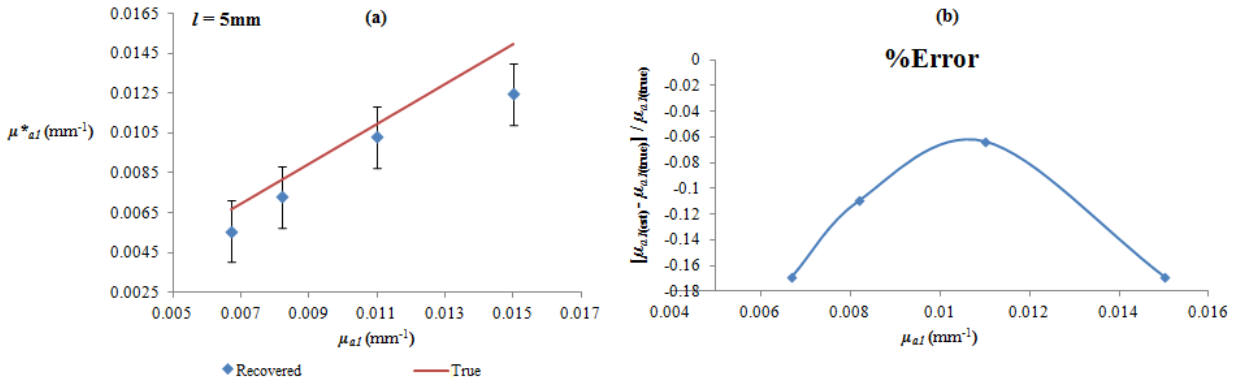

Figure 23 (a) Estimated absorption coefficients of the first layer (triangles) for a top layer thickness of 5mm obtained by nonlinear regression to simulated values of AC and phase for source-detector separations of 5mm to 10mm in 0.5mm increments using a solution of the diffusion equation for a semi-infinite homogeneous medium. The red line corresponds to the true value of $\boldsymbol{\mu_{a1}}$. (b) Error for the absorption coefficient calculated using Eq. (3.22)

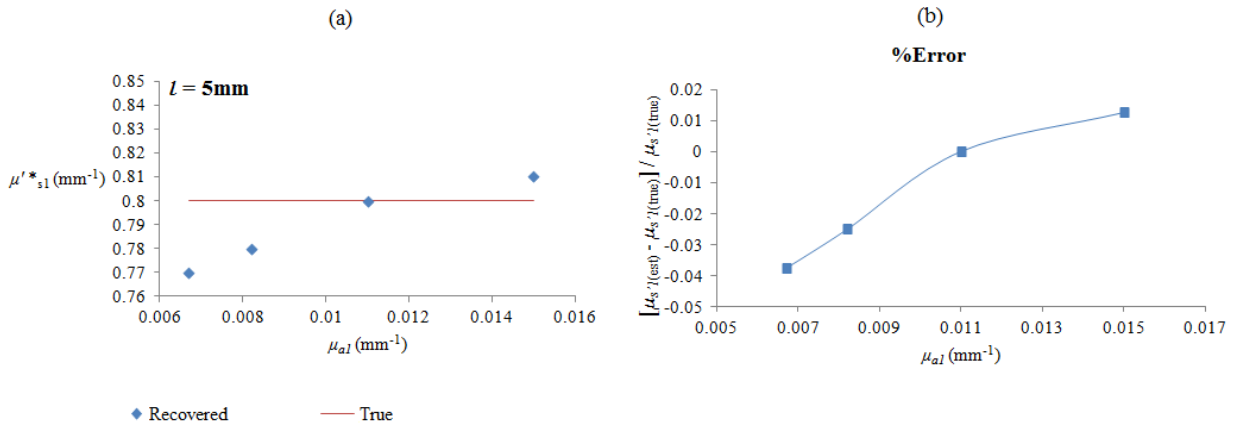

Figure 24 (a) Estimated reduced scattering coefficients of the first layer (diamonds) for a top layer thickness of 5mm obtained by nonlinear regression to simulated values of AC and phase for source-detector separations of 5mm to 10mm in 0.5mm increments using a solution of the diffusion equation for a semi-infinite homogeneous medium. The red line corresponds to the true value of $\boldsymbol{\mu'_{s1}}$. (b) Error for the reduced scattering coefficient calculated using Eq. (3.22)

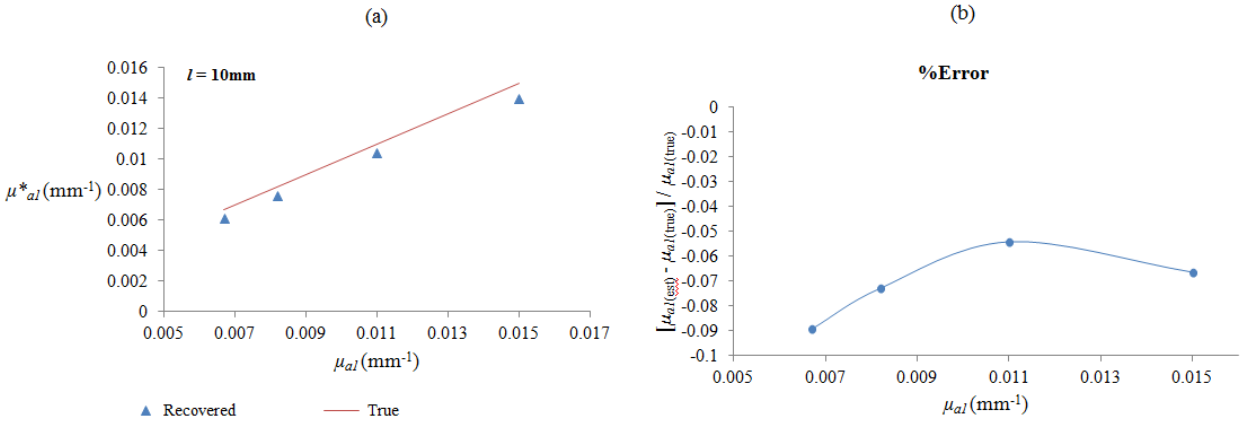

Figure 25 (a) Estimated absorption coefficients of the first layer (triangles) for a top layer thickness of 10mm obtained by nonlinear regression to simulated values of AC and phase for source-detector separations of 5mm to 10mm in 0.5mm increments using a solution of the diffusion equation for a semi-infinite homogeneous medium. The red line corresponds to the true value of $\boldsymbol{\mu_{a1}}$. (b) Error for the absorption coefficient calculated using Eq. (3.22)

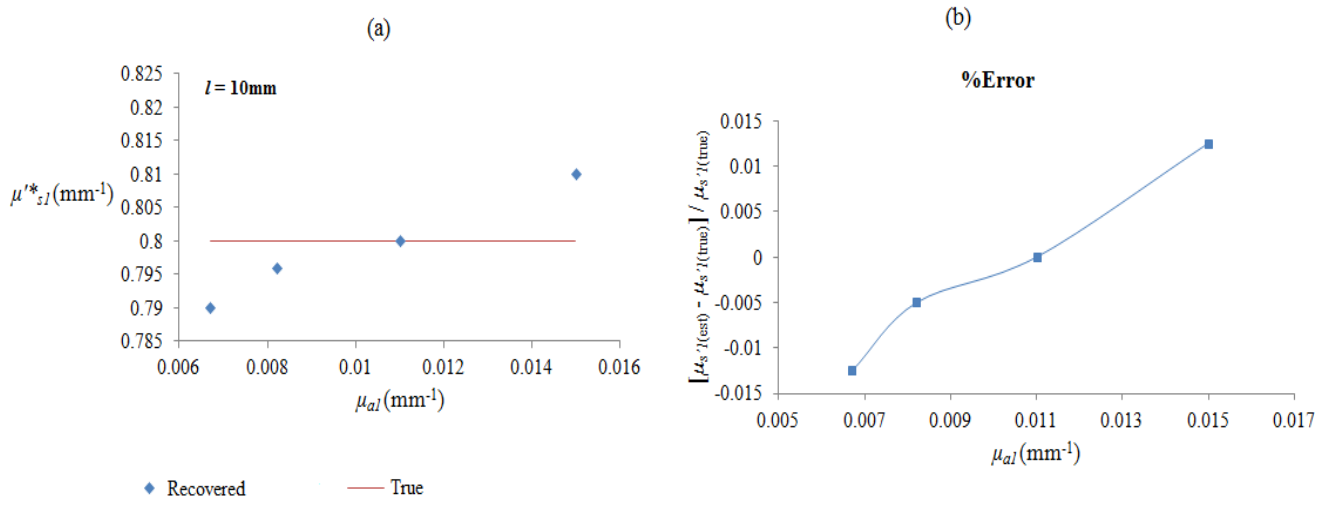

Figure 26 (a) Estimated reduced scattering coefficients of the first layer (diamonds) for a top layer thickness of 10mm obtained by nonlinear regression to simulated values of AC and phase for source-detector separations of 5mm to 10mm in 0.5mm increments using a solution of the diffusion equation for a semi-infinite homogeneous medium. The red line corresponds to the true value of $\boldsymbol{\mu'_{s1}}$. (b) Error for the reduced scattering coefficient calculated using Eq. (3.22)

3.3.2 Recovering μ_{a2} and μ'_{s2}

Using the optical properties of the first layer recovered in the manner described above as input alongside a known value of the superficial layer's thickness, μ_{a2} and μ'_{s2} were extracted by performing nonlinear regression to Monte Carlo-simulated data using the solutions of the diffusion equation for a two-layer model. A secant version of the Levenberg-Marquardt algorithm[13] is used in performing the nonlinear inversion to handle the differentiation with respect to μ_{a2} and μ'_{s2} numerically since the analytical expressions for the derivatives were both complicated and yielded inaccurate results. The absorption and reduced scattering coefficients for the brain (grey matter) in the NIR spectrum reported in the literature are taken as values for the initial guess $(\mu_{a2}^{(g)} = 0.01, \mu_{s2}^{\prime(g)} = 1)$ in the recovery procedure using the two-layer model. [14] The recovered values of μ_{a2} and μ'_{s2} are plotted in comparison with the true values and the effective parameters recovered by using the homogeneous model at source-detector spacing in the range 5mm to 60mm.

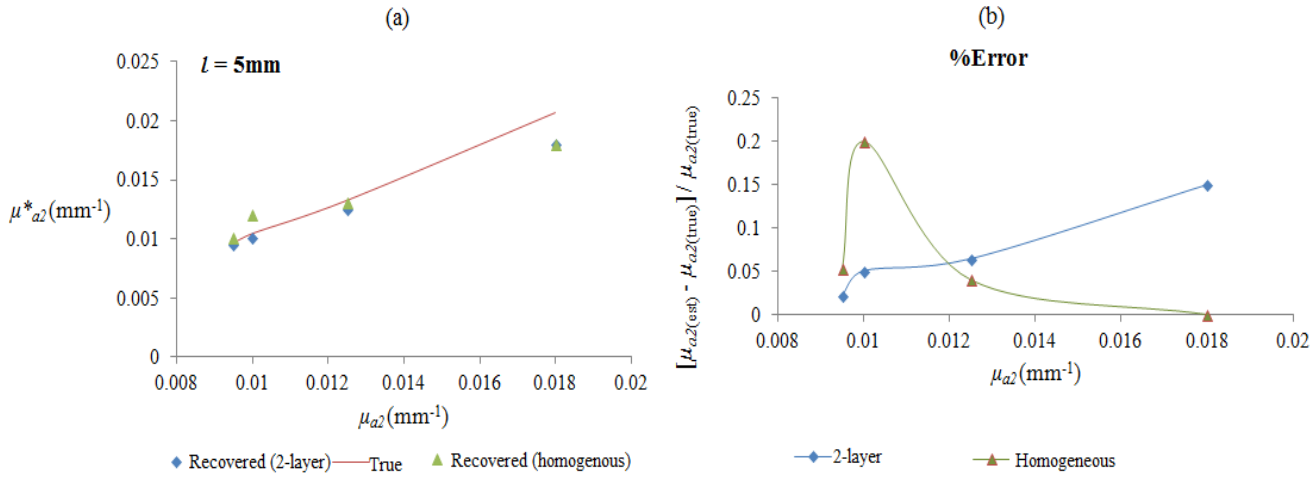

Figure 27 (a) Estimated absorption coefficients of the bottom layer (diamonds) for a top layer thickness of 5mm obtained by nonlinear regression to simulated values of AC and phase for source-detector separations of 5mm to 60mm using a solution of the diffusion equation for a two-layer medium. The absorption coefficient (triangles) estimated using the homogeneous model is also shown for comparison. The red line corresponds to the true value of $\boldsymbol{\mu_{a2}}$. (b) Error for the absorption coefficient calculated using Eq. (3.22)

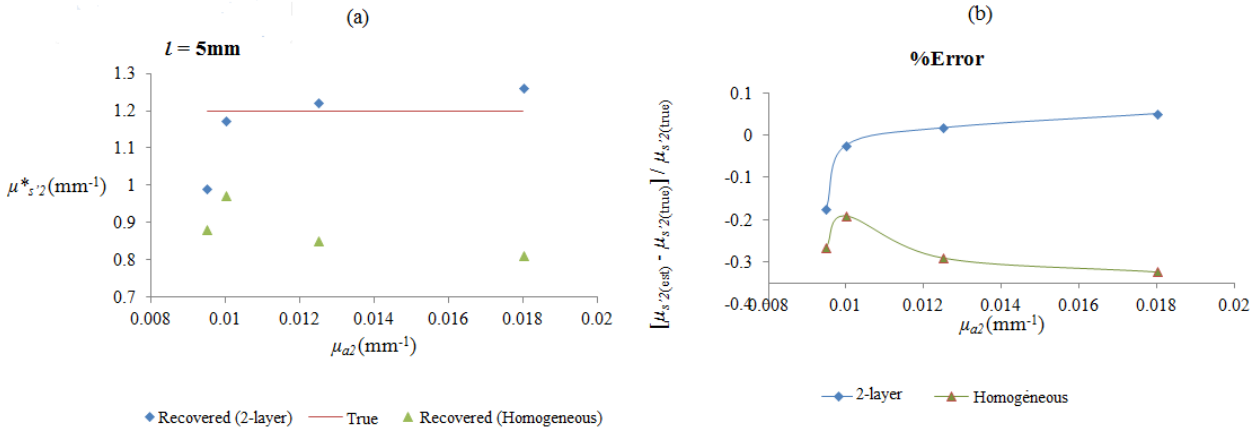

Figure 28 (a) Estimated reduced scattering coefficients of the bottom layer (diamonds) for a top layer thickness of 5mm obtained by nonlinear regression to simulated values of AC and phase for source-detector separations of 5mm to 60mm using a solution of the diffusion equation for a two-layer medium. The reduced scattering coefficient (triangles) estimated using the homogeneous model is also shown for comparison. The red line corresponds to the true value of $\boldsymbol{\mu_{s'2}}$. (b) Error for the reduced scattering coefficient calculated using Eq. (3.22)

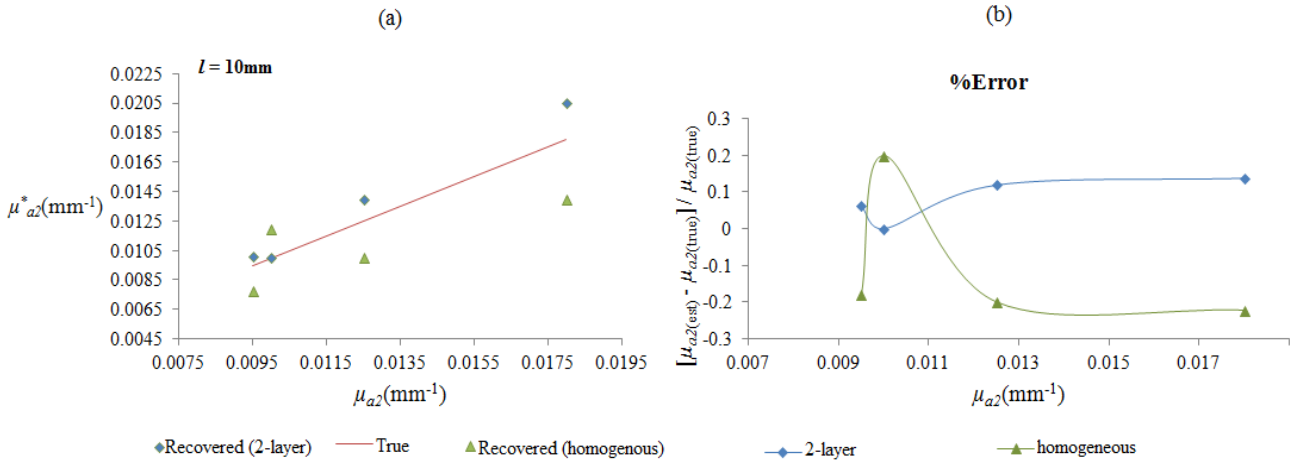

Figure 29 (a) Estimated absorption coefficients of the bottom layer (diamonds) for a top layer thickness of 10mm obtained by nonlinear regression to simulated values of AC and phase for source-detector separations of 5mm to 60mm using a solution of the diffusion equation for a two-layer medium. The absorption coefficient (triangles) estimated using the homogeneous model is also shown for comparison. The red line corresponds to the true value of $\boldsymbol{\mu_{a2}}$. (b) Error for the absorption coefficient calculated using Eq. (3.22)

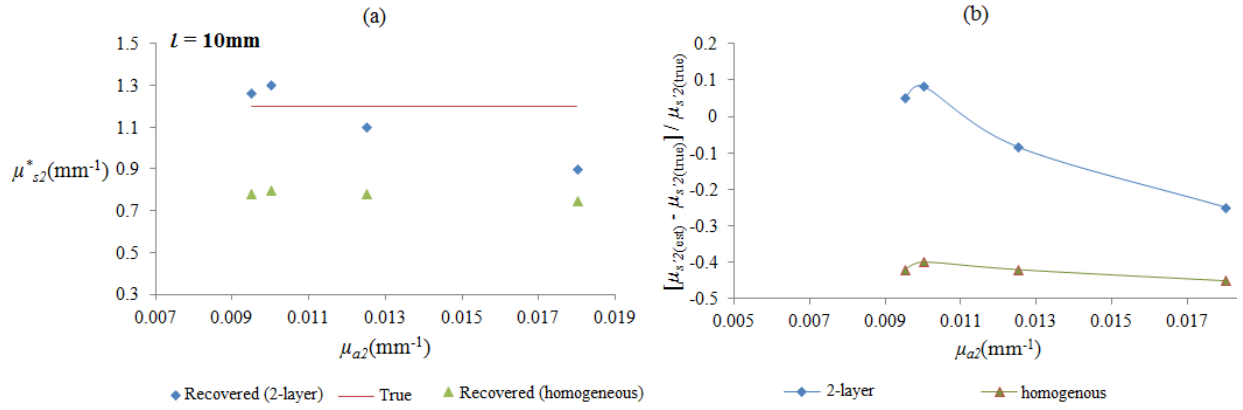

Figure 30 (a) Estimated reduced scattering coefficients of the bottom layer (diamonds) for a top layer thickness of 10mm obtained by nonlinear regression to simulated values of AC and phase for source-detector separations of 5mm to 60mm using a solution of the diffusion equation for a two-layer medium. The reduced scattering coefficient (triangles) estimated using the homogeneous model is also shown for comparison. The red line corresponds to the true value of $\boldsymbol{\mu_{s'2}}$. (b) Error for the reduced scattering coefficient calculated using Eq. (3.22)

3.3.3 Sensitivity to errors in l, μ_{a1} and μ'_{s1}

Although the Monte Carlo simulations were generated for known values of l and all four optical properties characterizing the two layers, knowledge of the exact values of these parameters when performing measurements on human subjects are not available at the outset.

However, recourse to compiled values in the literature provides a range where the actual values can be expected to lie. Moreover, the value of the thickness of the superficial layer can be ascertained from MRI images. Still, as the depth of the structures above the brain is non-uniform across the expanse of the human forehead and the optical properties of the superficial layer have been observed to vary among different people, it is worth looking at how the recovered values of μ_{a2} and $\mu_{s'2}$ are affected by uncertainties in l, μ_{a1} and $\mu_{s'1}$. (The optical properties employed in Tables 4 and 5 correspond to that listed under Case 4 in Table 3).

Table 4 Sensitiviy of recovered values to $\frac{\Delta l}{l} = \pm\mathbf{10}\%$, $\frac{\Delta\mu_{a1}}{\mu_{a1}} = \pm\mathbf{17}\%$, $\frac{\Delta\mu'_{s1}}{\mu'_{s1}} = \pm\mathbf{12}\%$ for a superficial layer thickness of 5mm

		$\frac{\Delta\mu'_{s1}}{\mu'_{s1}}$ = -12%		$\frac{\Delta\mu'_{s1}}{\mu'_{s1}}$= 0%		$\frac{\Delta\mu'_{s1}}{\mu'_{s1}}$= +12%	
	$\Delta\mu_{a1}/\mu_{a1}$	$\mu_{a2}^{(est)}(mm^{-1})$	$\mu_{s'2}^{(est)}(mm^{-1})$	$\mu_{a2}^{(est)}(mm^{-1})$	$\mu_{s'2}^{(est)}(mm^{-1})$	$\mu_{a2}^{(est)}(mm^{-1})$	$\mu_{s'2}^{(est)}(mm^{-1})$
$\Delta l/l$ = -10%	-17%	0.0096	1.42	0.0107	1.19	0.011	1.08
	0	0.0112	1.1	0.0106	1.12	0.011	1.04
	17%	0.01	1.19	0.0104	1.075	0.01	1.1
$\Delta l/l$ = 0%	-17%	0.0123	1.1	0.0104	1.24	0.011	1.1
	0	0.0093	1.38	0.0103	1.17	0.011	1.04
	17%	0.0106	1.1	0.0102	1.09	0.0105	1
$\Delta l/l$ = +10%	-17%	0.0127	1.1	0.01	1.32	0.011	1.12
	0	0.0115	1.1	0.01	1.18	0.0107	1.05
	17%	0.0091	1.3	0.01	1.1	0.0104	1.00

Table 5 Sensitivity of recovered values to $\frac{\Delta l}{l} = \pm\mathbf{10}\%$, $\frac{\Delta\mu_{a1}}{\mu_{a1}} = \pm\mathbf{17}\%$, $\frac{\Delta\mu'_{s1}}{\mu'_{s1}} = \pm\mathbf{12}\%$ for a superficial layer thickness of 10mm

		$\frac{\Delta\mu'_{s1}}{\mu'_{s1}}$ = -12%		$\frac{\Delta\mu'_{s1}}{\mu'_{s1}}$= 0%		$\frac{\Delta\mu'_{s1}}{\mu'_{s1}}$= +12%	
	$\Delta\mu_{a1}/\mu_{a1}$	$\mu_{a2}^{(est)}(mm^{-1})$	$\mu_{s2}^{\prime(est)}(mm^{-1})$	$\mu_{a2}^{(est)}(mm^{-1})$	$\mu_{s2}^{\prime(est)}(mm^{-1})$	$\mu_{a2}^{(est)}(mm^{-1})$	$\mu_{s2}^{\prime(est)}(mm^{-1})$
$\Delta l/l$ = -10%	-17%	0.018	1.1	0.013	1.1	0.014	0.84
	0	0.0082	2	0.011	0.98	0.01	1.1
	17%	0.01	1.1	0.0096	1.1	0.01	1.1
$\Delta l/l$ = 0%	-17%	0.022	1.1	0.014	1.1	0.014	0.83
	0	0.013	1.1	0.011	1.2	0.013	0.71
	17%	0.008	1.50	0.011	0.8	0.011	1.08
$\Delta l/l$ = +10%	-17%	0.03	1.1	0.015	1.1	0.012	1.1
	0	0.014	1.1	0.01	1.1	0.01	1.1
	17%	0.0093	1.1	0.0088	1.1	0.01	1.1

3.4 Discussion

The values of AC and phase obtained by implementing the two-layer forward model were compared with those from Monte Carlo simulations for source-detector distances in the range 5mm-60mm. The same solution was implemented to recover the optical properties of the bottom layer using the multi-distance method in the frequency domain for a modulation frequency of 110MHz. The values of the bottom layer's optical properties recovered by the two-layer model and the homogenous semi-infinite model are also compared. In both models, the banana-shaped light bundle samples tissue volume residing at greater depths at large source-detector distances. However, they differ mainly in two aspects: the two-layer model separates the contribution of each layer to the collected optical signal whereas in the homogenous model, the optical data is attributable to effective universal values of μ_a and μ_s' with distinctions between heterogeneous tissue domains being less apparent. The results demonstrate that the optical properties of deeper regions are better extracted using a model that accounts for the heterogeneity in μ_a and μ_s' due to the layered structure of tissue. Looking at the results in subsection 3.3.2, the effective values recovered for μ_{a2} and μ_{s2}' using the solution to the diffusion equation for a homogeneous medium at large source-detector separations are an average between that of the top and bottom layer's. Lastly, the recovery of μ_{a2} and μ_{sr2} was examined for sensitivity to errors in l, μ_{a1} and μ_{s1}' since there is always some degree of uncertainty in these quantities in measurement scenarios. Although these differences are due to the influence of the structures directly above the brain, foreheads with thin superficial layers possess a lesser degree of non-uniformity in tissue architecture and are therefore relatively homogeneous as opposed to those with thicker layers. This can be seen Figure 27a where l=5mm and no significant departures from the true values in the recovered absorption coefficient of the bottom layer were observed using the homogeneous model. However, for foreheads with thicker superficial layers, the layered anatomy of tissue with the concomitant contrast in μ_a (Fig 29a) and μ_s' (Fig 30a) between the two layers become more pronounced and recourse to a layered model of tissue becomes necessary. These results are

consistent with phantom studies that investigated the influence of the top layer in the recovering the optical parameters of the bottom layer. [12]

The influence of uncertainties in the thickness of the superficial layer and the optical properties of the first layer on the recovered value of μ_{a2} and $\mu_{s'2}$ were investigated as well. For a two-layer medium with a top layer thickness of 5mm, it can be seen that overestimating μ_{a1} (l) by 17% (10%) and underestimating $\mu_{s\prime 1}$ by 12% yield values of $\mu_{a2}^{(est)}$ that are within 9% of their true values. However, underestimating μ_{a1} and μ_{s1}' by 17% and 12% respectively give a $\mu_{a2}^{(est)}$ that is 23% greater than its true value. This increases to 27% when μ_{a1} and $\mu_{s\prime 1}$ are underestimated by 17% and 12% respectively while overestimating l by 10%. As for the recovered scattering coefficient of the bottom layer, underestimating $\mu_{a1,}$ $\mu_{s\prime 1}$ and l by 17%, 12% and 10% respectively can recover μ_{s2}' to within ~18% of its true value. For an upper-layer thickness of 10mm, $\mu_{a2}^{(est)}$ is 20% of its true value if $\mu_{s\prime 1}$ is underestimated 12%. On the other hand, $\mu_{a2}^{(est)}$ rises to 30% above its true value when l is underestimated by 10% while remaining insensitive to μ_{a1} and $\mu_{s\prime 1}$ when both are underestimated by 17% and 12% respectively. In addition, $\mu_{s\prime 2}^{(est)}$ was observed to be sensitive to errors in l and $\mu_{s\prime 1}$; the error in its recovered value was ~41% when $\mu_{s\prime 1}$ was overestimated by 12% and ~67% when l was underestimated by 10%. This is highlighted furthermore by the fact that even if one of the three parameters is known with absolute certainty, the reduced scattering coefficient of the bottom layer is bound to be overestimated more than 20% due to variations in the other two. By comparison, $\mu_{s\prime 2}^{(est)}$remains relatively stable when $\mu_{s\prime 1}$ is known with absolute certainty. The results are summarized in Table 4 and Table 5

The uncertainties in l, μ_{a1} and $\mu_{s'1}$ are taken from reported values in literature. The $\pm$10% error in l is due to the uncertainty of 1mm^3 in the voxel size in MRI images.[15] The $\pm$12% and $\pm$17% uncertainty in the reduced scattering and absorption coefficients, respectively, correspond to errors obtained from measurements made on phantoms that were customized to mimic the optical properties of the scalp-skull region.[16] These choices for the errors in μ_{a1} and μ_{s1}' also reflect the uncertainty that one

would expect from experimental measurements on a real forehead when close distances ($\rho \leq$10mm) are considered.

3.5 Conclusion and future directions

A two-layer model of the human forehead has been studied with a view to determining the absorption and reduced scattering coefficients of the brain. It was found that for thin superficial layer thicknesses (l = 5mm), the utility of the homogeneous model in recovering μ_a of the bottom layer at large source-detector distances is not significantly different from when the two-layer model is employed (see Fig 27a). However, the two-layer model exhibited better sensitivity to contrast in $\mu_{s\prime}$, for a layered medium than the homogeneous model (see Fig 28a). However, as Figures 29 and 30 illustrate, the difference between the two models in recovering μ_a and $\mu_{s\prime}$ of the bottom layer becomes evident for thicker superficial layers (l = 10mm). In addition, it was found that the sensitivity of the recovery procedure to errors in the optical properties and thickness of the first layer was more apparent for a two-layer system with $l = 10mm$ (see Table 5).

A model that accounts for the heterogeneity of optical properties of tissue has made possible a better quantification of the changes in physiologically relevant parameters indicative of tissue health and function.[16] The values of μ_a and $\mu_{s\prime}$ recovered by regressing theoretical values of AC and phase from the semi-infinite homogeneous model to those obtained from Monte Carlo simulations include partial contributions from both layers. This precludes measurement of the native absorption and scattering properties of what in actuality are physically demarcated regions. This shortcoming diminishes the diagnostic utility of the homogenous model in extracting the optical properties of deep-seated tissue regions. Previous studies that sought to recover all 5 parameters using the two-layer model -- μ_a and $\mu_{s\prime}$ of the two layers together with l – have remarked on the potential ill-posedness of this model.[17],[18] The existence of several solutions minimizing χ^2 pose a limitation on the utility of the two-layer model in determining the absorption and reduced scattering properties of both layers and deserves further

investigation. Regularization techniques are known to handle systems that are ill-posed and so may provide a way of recovering all 5 parameters simultaneously.[19]

Recent investigations have been carried out to determine the effect of the cerebrospinal fluid (CSF) and head curvature in both infants and adults in extracting μ_a and $\mu_{s\prime}$.[20] The influence of the CSF layer and the curvature of the head may also provide an additional refinement to layered tissue model just investigated. In this study, both are ignored to favor an even surface corresponding to the forehead. The greater curvature of the head among infants due to its small size effectively places a limit on the possible range of source-detector distances that can be used such that the tissue-air interface can be considered flat. In addition, although the contribution of the CSF is minimal, its presence in high amounts effectively introduces another layer and could present errors in extracting [Hb] and [HbO] in the inversion procedure.

In another recent study, frequency domain measurements that make use of the multi-distance configuration have recently been carried out by Hallacoglu *et al.*(2011) out to examine differences in cerebral perfusion between rats that were fed a folate-deficient diet and those (control) whose diet had adequate folate content.[21] In contrast to relative measurements, the technique used in this study had the distinguishing feature of being able to perform absolute measurements of baseline hemoglobin concentration in cerebral tissue. A key finding of the study was the onset of cognitive impairment in association with folate deficiency. With respect to the control group, folate-deficient rats had lower baseline concentrations of cerebral oxyhemoglobin [HbO], total hemoglobin [HbT] and oxygen saturation [StO_2]. The parallel reduction in cerebral perfusion observed among those suffering from Alzheimer's disease and the degree to which lower baseline values of the physiological parameters ([HbO],[HbT] and [StO_2]) may serve as an indicator of cognitive dysfunction may therefore be investigated using NIRS.

Applying a two-layer model of the head could provide an avenue for further refining the recovered optical properties of the brain by separating the contribution of the extracerebral layer to the collected optical signal.

Chapter 3 References

[1] I. Lux and L. Koblinger, Monte Carlo Particle Transport Methods: Neutron and Photon Calculations (CRC Press, Boca Raton, FL, 1991).

[2] A. Sassaroli, Fundamental studies of near Infrared spectroscopy and diffuse optical tomography for biomedical diagnosis. PhD thesis, University of Electro-Communication in Tokyo, Japan, 2002

[3] L. Wang, S.L. Jacques, and L. Zheng,"MCML-Monte Carlo modeling of light transport in multi-layered tissues," Comput. Methods Programs Biomed. 47, 131-146 (1995).

[4] R. Shiavi, Introduction to applied statistical signal analysis (Academic Press, San Diego, 1999). Chapter 2.

[5] Weisstein, Eric W. "Probability Density Function." From MathWorld--A Wolfram Web Resource. http://mathworld.wolfram.com/ProbabilityDensityFunction.html

[6] A. Ishimaru, Wave Propagation and Scattering in Random Media (Academic, New York, 1997). Chapter 7.

[7] T. Durduran, R. Choe, WB Baker, and AG Yodh, "Diffuse optics for tissue monitoring and tomography," Rep. Prog. Phys. 73 (2010)

[8] A. Sassaroli, F. Martelli, and S. Fantini, "Perturbation theory for the diffusion equation by use of the moments of the generalized temporal point spread function. III. Frequency-domain and time-domain results," J. Opt. Soc. Am. 7, 1723-1742 (2010)

[9] A. Kienle and T. Glanzmann, "In vivo determination of the optical properties of muscle with time-resolved reflectance using a layered model," Phys. Med. Biol 44, 2689-2702 (1999).

[10] R. Ankri, H. Taitelbaum and D. Fixler, “Reflected light intensity profiles of two-layer tissues: phantom experiments,” 16, 1-6 (2011)

Delete this part [11] E. Okada, M. Firbank and D.T. Delpy, “The effect of overlying tissue on the spatial sensitivity profile of near-infrared spectroscopy,” Phys. Med. Biol. 40, 2093-2108 (1995)

[11] A. Kienle, T. Glanzmann, M.S. Patterson, N. Utke, R. Bays, G. Wagniéres, and H. van der Bergh, ”Noninvasive determination of the optical properties of two-layered turbid media,” Appl. Opt. 37, 779-791 (1998)

[12] M.A. Franceschini, S. Fantini, L.A. Paunescu, J.S. Maier, and E. Gratton, “Influence of a superficial layer in the quantitative spectroscopic study of strongly scattering media,” Applied Optics 37, 7447-7458 (1998)

[13] K. Madsen, H.B. Nielsen, and O. Tingleff, Methods for non-linear least squares problems (Technical University of Denmark, 2004)

[14] A.N. Yaroslavsky, P.C. Schulze, I.V. Yaroslavsky, R. Schober, F. Ulrich, and H.J. Scwarzmaier, “Optical properties of selected native and coagulated human brain tissues in vitro in the visible and near infrared spectral range,” Phys. Med. Biol. 47, 2059-2073 (2002).

[15] L. Gagnon, C. Gauthier, R.D. Hoge, F. Lesage, J. Selb and D.A. Boas, “Double-layer estimation of intra- and extracerebral hemoglobin concentration with a time-resolved system,” Journal of Biomedical Optics 13, 1-9 (2008).

[16] Y.S. Fawzi, A.M. Youssef, M.H. El-Batanony, and Y.M. Kadah, “Determination of the optical properties of a two-layer tissue model by detecting photons migrating at progressively increasing depths,” Applied Optics 42, 6398-6411 (2003)

[17] J. Choi, M. Wolf, V. Toronov, U. Wolf, C. Polzonetti, D. Hueber, L.P. Safonova, R. Gupta, A. Michalos, W. Mantulin, E. Gratton, "Noninvasive determination of the optical properties of adult brain: near-infrared spectroscopy approach," Journal of Biomedical Optics 9, 221-229 (2004)

[18] T.H. Pham, T. Spott, L.O. Svaasand, and B.J. Tromberg, "Quantifying the properties of two-layer turbid media with frequency-domain diffuse reflectance," Applied Optics 39, 4733-4745 (2000).

[19] R.C. Aster, B. Borchers, and C.H. Thurber, Parameter Estimation and Inverse Problems. (Elsevier Academic Press, Burlington, MA, 2005). Chapter 5.

[20] M/ Dehaes, P.E. Grant, D.D. Sliva, N. Roche-Labarbe, R. Pienaar, D. A. Boas, M.A. Franceschini, and J. Selb, "Assessment of the frequency-domain multi-distance method to evaluate the brain optical properties: Monte Carlo simulations from neonate to adult," Biomedical Optics Express 2, 552-567 (2011).

[21] B. Hallacoglu, A. Sassaroli, S. Fantini, and A.M. Troen, "Cerebral perfusion and oxygenation are impaired by folate deficiency in rat: absolute measurements with noninvasive near-infrared spectroscopy," Journal of Cerebral Blood Flow & Metabolism 31, 1482-1492 (2011)

Appendix A: Derivation of the Solutions to the Diffusion Equation for a Two-Layered Turbid Media

For the two-layer model, the diffusion equation for the two layers give:

$$D_1\nabla^2\,\Psi_1(\mathbf{r}) - \,(\mu_{a1} + \frac{i\omega}{c})\Psi_1(\mathbf{r}) = \,-\delta(x,y,z-z_o) \qquad 0 \le z < l \qquad \text{(A1)}$$

$$D_2\nabla^2\,\Psi_2(\mathbf{r}) - \,(\mu_{a2} + \frac{i\omega}{c})\Psi_2(\mathbf{r}) = \,0 \qquad l \le z \qquad \text{(A2)}$$

A two-dimensional Fourier transform is then applied to Eq (A1) and (A2) to transform them into ordinary differential equations:

$\varphi_k(z,s_1,s_2) = \int_{-\infty}^{\infty}\int_{-\infty}^{\infty}\Psi_k(x,y,z)e^{k(s_1x+s_2y)}dxdy$ where *k* denotes the k^{th} layer.

For the first layer,

$$\boldsymbol{\mathcal{F}}\left\{D_1\nabla^2\,\Psi_1(\mathbf{r}) - \,(\mu_{a1} + \frac{i\omega}{c})\Psi_1(\mathbf{r})\right\} = \,\boldsymbol{\mathcal{F}}\{-\delta(x,y,z-z_o)\}. \qquad \text{(A3)}$$

From the linearity of the Fourier transform, (A3) becomes,

$$D_1\boldsymbol{\mathcal{F}}[\nabla^2\,\Psi_1(\mathbf{r})] - (\mu_{a1} + \frac{i\omega}{c})\boldsymbol{\mathcal{F}}[\Psi_1(\mathbf{r})] = \,-\boldsymbol{\mathcal{F}}[\delta(x,y,z-z_o)]. \qquad \text{(A4)}$$

Applying the definition of the Laplacian,

$$D_1\boldsymbol{\mathcal{F}}[\frac{\partial^2\Psi_1(\mathbf{r})}{\partial \mathrm{x}^2} + \frac{\partial^2\Psi_1(\mathbf{r})}{\partial \mathrm{y}^2} + \frac{\partial^2\Psi_1(\mathbf{r})}{\partial \mathrm{z}^2}] - (\mu_{a1} + \frac{i\omega}{c})\boldsymbol{\mathcal{F}}[\Psi_1(\mathbf{r})] = \,-\boldsymbol{\mathcal{F}}[\delta(x,y,z-z_o)]. \qquad \text{(A5)}$$

The Fourier transform an n^{th} order derivative allows us to obtain the transformed components of the Laplacian. We note that:

$$\boldsymbol{\mathcal{F}}\left[\frac{d^n}{dy^n}x(y)\right] = (is)^n X(is). \qquad \text{(A6)}$$

Applying this to each of the terms of the Laplacian gives:

$$D_1\left[(is_1)^2\varphi_1(z,s)+(is_2)^2\varphi_1(z,s)+\frac{\partial^2\varphi_1(z,s)}{\partial z^2}\right]-\left(\mu_{a1}+\frac{i\omega}{c}\right)\varphi_1(z,s)=-\delta(z-z_o) \quad \text{(A7)}$$

Re-arranging,

$$-(s_1^2+s_2^2)\varphi_1(z,s)-\frac{1}{D_1}\left(\mu_{a1}+\frac{i\omega}{c}\right)\varphi_1(z,s)+\frac{\partial^2\varphi_1(z,s)}{\partial z^2}=\frac{-\delta(z-z_o)}{D_1}$$

Letting $s^2 = s_1^2 + s_2^2$,

$$\frac{\partial^2\varphi_1(z,s)}{\partial z^2}-\left\{\frac{1}{D_1}\left[\left(\mu_{a1}+\frac{i\omega}{c}\right)+D_1s^2\right]\right\}\varphi_1(z,s)=\frac{-\delta(z-z_o)}{D_1} \quad \text{(A8)}$$

This reproduces Eq. (2.13) with $\alpha_1^2=\frac{1}{D_1}\left[\left(\mu_{a1}+\frac{i\omega}{c}\right)+D_1s^2\right]$. Applying the same procedure to (A2) gives Eq. (2.14). The ordinary differential equations obtained after performing the 2D Fourier transform are re-stated:

$$\frac{\partial^2\varphi_1(z,s)}{\partial z^2}-\alpha_1^2\varphi_1(z,s)=-\frac{\delta(z-z_o)}{D_1} \qquad 0\le z<l$$

$$\frac{\partial^2\varphi_2(z,s)}{\partial z^2}-\alpha_2^2\varphi_2(z,s)=0 \qquad l\le z$$

The general solutions of Eq. (2.13) and Eq. (2.14) are given by: [24]

$$\varphi_1(0<z<z_o,s)=A_1e^{-\alpha_1z}+B_1e^{\alpha_1z} \quad \text{(A9)}$$

$$\varphi_1(z_o<z<l,s)=C_1e^{-\alpha_1z}+E_1e^{\alpha_1z} \quad \text{(A10)}$$

$$\varphi_2(l\le z,s)=A_2e^{-\alpha_2z}+B_2e^{\alpha_2z} \quad \text{(A11)}$$

To solve Eq (2.13) and (2.14), the following boundary conditions (BCs) are employed:

$$\varphi_1(-z_b,s)=0 \quad \text{(A12)}$$

$$\varphi_2(\infty, s) = 0 \tag{A13}$$

$$\frac{\varphi_1(l,s)}{\varphi_2(l,s)} = \frac{n_1^2}{n_2^2} = 1 \tag{A14}$$

$$D_1 \frac{\partial \varphi_1(z,s)}{\partial z}|_{z=l} = D_2 \frac{\partial \varphi_2(z,s)}{\partial z}|_{z=l} \tag{A15}$$

Where Eq.(A12) is the extrapolated boundary condition.

Noting the continuity of φ_1,

$$\varphi_1(z_o < z < l) = \varphi_1(0 < z < z_o) \tag{A16}$$

The discontinuity of the derivative of the dirac delta function yields:

$$-D_1 z \frac{\partial \varphi_1}{\partial z}\Big|_{z_o<z<l} + -D_1 z \frac{\partial \varphi_1}{\partial z}\Big|_{0<z<z_o} = 1 \tag{A17}$$

From Eq. (A13), we immediately see that $B_2 = 0$. Therefore,

$$\varphi_2(l \leq z, s) = A_2 e^{-\alpha_2 z} \tag{A18}$$

Similarly, considering the conditions stipulated in Eq (A12) and Eqs.(A13-A17), the following system of equations are obtained:

$$A_1 e^{\alpha_1 z_b} + B_1 e^{-\alpha_1 z_b} = 0 \tag{A19}$$

$$A_1 e^{-\alpha_1 z_o} + B_1 e^{\alpha_1 z_o} = C_1 e^{-\alpha_1 z_o} + E_1 e^{\alpha_1 z_o} \tag{A20}$$

$$-D_1(-\alpha_1 C_1 e^{-\alpha_1 z_o} + \alpha_1 E_1 e^{\alpha_1 z_o}) + D_1(-\alpha_1 A_1 e^{-\alpha_1 z_o} + \alpha_1 B_1 e^{\alpha_1 z_o}) = 1 \tag{A21}$$

$$C_1 e^{-\alpha_1 l} + E_1 e^{\alpha_1 l} = A_2 e^{-\alpha_2 l} \tag{A22}$$

$$D_1\left(-\alpha_1 C_1 e^{-\alpha_1 l} + \alpha_1 E_1 e^{\alpha_1 l}\right) = D_2(-\alpha_2 A_2 e^{-\alpha_2 l}) \tag{A23}$$

Eq. (A19) immediately gives

$$A_1 = -B_1 e^{-2\alpha_1 z_b} \tag{A24}$$

Substituting this into Eq (A20) yields,

$$-B_1 e^{-\alpha_1(2z_b+z_o)} + B_1 e^{\alpha_1 z_o} = C_1 e^{-\alpha_1 z_o} + E_1 e^{\alpha_1 z_o} \tag{A25}$$

Solving for B_1,

$$B_1 = \frac{C_1 e^{-\alpha_1 z_o} + E_1 e^{\alpha_1 z_o}}{e^{\alpha_1 z_o} - e^{-\alpha_1(2z_b+z_o)}} \tag{A26}$$

Inserting A_1 and B_1 to Eq. (A21) gives,

$$-D_1(-\alpha_1 C_1 e^{-\alpha_1 z_o} + \alpha_1 E_1 e^{\alpha_1 z_o}) + D_1\alpha_1\left[\frac{e^{-\alpha_1(2z_b+z_o)} + e^{\alpha_1 z_0}}{e^{\alpha_1 z_o} - e^{-\alpha_1(2z_b+z_o)}}\right](C_1 e^{-\alpha_1 z_o} + E_1 e^{\alpha_1 z_o}) = 1 \tag{A27}$$

Re-grouping,

$$C_1 e^{-\alpha_1 z_o}\left(1 + \left[\frac{e^{-\alpha_1(2z_b+z_o)} + e^{\alpha_1 z_0}}{e^{\alpha_1 z_o} - e^{-\alpha_1(2z_b+z_o)}}\right]\right) + E_1\left(\left[\frac{e^{-\alpha_1(2z_b+z_o)} + e^{\alpha_1 z_0}}{e^{\alpha_1 z_o} - e^{-\alpha_1(2z_b+z_o)}}\right] - 1\right) = \frac{1}{\alpha_1 D_1} \tag{A28}$$

Solving for C_1,

$$C_1 = \frac{e^{\alpha_1 z_o} - e^{-\alpha_1(2z_b+z_o)}}{2\alpha_1 D_1} - E_1 e^{-2\alpha_1 z_b} \tag{A29}$$

Substituting C_1 to Eq. (A22) gives,

$$\left(\frac{e^{\alpha_1 z_o} - e^{-\alpha_1(2z_b+z_o)}}{2\alpha_1 D_1} - E_1 e^{-2\alpha_1 z_b}\right) e^{-\alpha_1 l} + E_1 e^{\alpha_1 l} = A_2 e^{-\alpha_2 l} \tag{A30}$$

Re-arrangement yields,

$$E_1(e^{\alpha_1 l} - e^{-\alpha_1(2z_b+l)}) = A_2 e^{-\alpha_2 l} + \frac{e^{-\alpha_1(2z_b+z_o+l)} - e^{\alpha_1(z_o-l)}}{2\alpha_1 D_1} \tag{A31}$$

Solving for E_1gives

$$E_1 = \frac{1}{(e^{\alpha_1 l} - e^{-\alpha_1(2z_b+l)})}\left(A_2 e^{-\alpha_2 l} + \frac{e^{-\alpha_1(2z_b+z_o+l)} - e^{\alpha_1(z_o-l)}}{2\alpha_1 D_1}\right) \quad \text{(A33)}$$

Re-ordering Eq. (A23),

$$-C_1 e^{-\alpha_1 l} + E_1 e^{\alpha_1 l} = -\frac{\alpha_2 D_2}{\alpha_1 D_1} A_2 e^{-\alpha_2 l} \quad \text{(A34)}$$

Inserting C_1 and E_1 yields

$$\frac{e^{\alpha_1 l} + e^{-\alpha_1(2z_b+l)}}{e^{\alpha_1 l} - e^{-\alpha_1(2z_b+l)}}\left(A_2 e^{-\alpha_2 l} + \frac{e^{-\alpha_1(2z_b+z_o+l)} - e^{\alpha_1(z_o-l)}}{2\alpha_1 D_1}\right) + \frac{e^{-\alpha_1(2z_b+z_o+l)} - e^{\alpha_1(z_o-l)}}{2\alpha_1 D_1} = -\frac{\alpha_2 D_2}{\alpha_1 D_1} A_2 e^{-\alpha_2 l} \quad \text{(A35)}$$

Grouping the coefficients of A_2,

$$A_2 e^{-\alpha_2 l}\left(\frac{e^{\alpha_1 l} + e^{-\alpha_1(2z_b+l)}}{e^{\alpha_1 l} - e^{-\alpha_1(2z_b+l)}} + \frac{\alpha_2 D_2}{\alpha_1 D_1}\right) + \frac{1}{\alpha_1 D_1}\left(\frac{e^{-\alpha_1(2z_b+z_o)} - e^{\alpha_1 z_o}}{e^{\alpha_1 l} - e^{-\alpha_1(2z_b+l)}}\right) = 0 \quad \text{(A36)}$$

Multiplying both sides by $\alpha_1 D_1(e^{\alpha_1 l} - e^{-\alpha_1(2z_b+l)})$,

$$A_2 e^{-\alpha_2 l}\left[\alpha_1 D_1\left(e^{\alpha_1 l} + e^{-\alpha_1(2z_b+l)}\right) + \alpha_2 D_2(e^{\alpha_1 l} - e^{-\alpha_1(2z_b+l)})\right] + e^{-\alpha_1(2z_b+z_o)} - e^{\alpha_1 z_o} = 0 \quad \text{(A37)}$$

Solving for A_2,

$$A_2 = e^{\alpha_2 l}\left(\frac{e^{\alpha_1 z_o} - e^{-\alpha_1(2z_b+z_o)}}{\alpha_1 D_1\left(e^{\alpha_1 l} + e^{-\alpha_1(2z_b+l)}\right) + \alpha_2 D_2(e^{\alpha_1 l} - e^{-\alpha_1(2z_b+l)})}\right) \quad \text{(A38)}$$

Factoring out $e^{-\alpha_1 z_b}$ and re-positioning it in the numerator gives,

$$A_2 = e^{\alpha_2 l}\left(\frac{e^{\alpha_1(z_o+z_b)} - e^{-\alpha_1(z_b+z_o)}}{\alpha_1 D_1\left(e^{\alpha_1(z_b+l)} + e^{-\alpha_1(z_b+l)}\right) + \alpha_2 D_2(e^{\alpha_1(z_b+l)} - e^{-\alpha_1(z_b+l)})}\right) \quad \text{(A39)}$$

By $\sinh x = \frac{e^x - e^{-x}}{2}$ and $\cosh x = \frac{e^x + e^{-x}}{2}$,

$$A_2 = \frac{\sinh[\alpha_1(z_o+z_b)]e^{\alpha_2 l}}{\alpha_1 D_1 \cosh[\alpha_1(l+z_b)] + \alpha_2 D_2 \sinh[\alpha_1(l+z_b)]} \quad \text{(A40)}$$

Inserting A_2 into the solution for the second layer,

$$\boxed{\varphi_2(z,s) = \frac{\sinh[\alpha_1(z_o+z_b)]e^{\alpha_2(l-z)}}{\alpha_1 D_1 \cosh[\alpha_1(l+z_b)]+\alpha_2 D_2 \sinh[\alpha_1(l+z_b)]}} \quad \text{(A41)}$$

Working back to obtain the other constants, A_2 is substituted into the expression for E_1 and C_1 ,

$$E_1 = \frac{1}{(e^{\alpha_1 l}-e^{-\alpha_1(2z_b+l)})}\left(\frac{\sinh[\alpha_1(z_o+z_b)]}{\alpha_1 D_1 \cosh[\alpha_1(l+z_b)]+\alpha_2 D_2 \sinh[\alpha_1(l+z_b)]} + \frac{e^{-\alpha_1(2z_b+z_o+l)}-e^{\alpha_1(z_o-l)}}{2\alpha_1 D_1}\right) \quad \text{(A42)}$$

$$C_1 =$$

$$\frac{e^{\alpha_1 z_o}-e^{-\alpha_1(2z_b+z_o)}}{2\alpha_1 D_1} - \left(\frac{e^{-2\alpha_1 z_b}}{(e^{\alpha_1 l}-e^{-\alpha_1(2z_b+l)})}\left(\frac{\sinh[\alpha_1(z_o+z_b)]}{\alpha_1 D_1 \cosh[\alpha_1(l+z_b)]+\alpha_2 D_2 \sinh[\alpha_1(l+z_b)]} + \frac{e^{-\alpha_1(2z_b+z_o+l)}-e^{\alpha_1(z_o-l)}}{2\alpha_1 D_1}\right)\right)$$

(A43)

Substituting E_1 and C_1 into Eq. (A10),

$$\varphi_1(z_o < z < l, s) = \frac{e^{-\alpha_1(z-z_o)}-e^{-\alpha_1(2z_b+z_o+z)}}{2\alpha_1 D_1} + \frac{e^{\alpha_1 z}-e^{-\alpha_1(2z_b+z)}}{e^{\alpha_1 l}-e^{-\alpha_1(2z_b+l)}}\left(\frac{\sinh[\alpha_1(z_o+z_b)]}{\alpha_1 D_1 \cosh[\alpha_1(l+z_b)]+\alpha_2 D_2 \sinh[\alpha_1(l+z_b)]} + \frac{e^{-\alpha_1(2z_b+z_o+l)}-e^{\alpha_1(z_o-l)}}{2\alpha_1 D_1}\right) \quad \text{(A44)}$$

For convenience, we set $\beta = \alpha_1 D_1 \cosh[\alpha_1(l+z_b)] + \alpha_2 D_2 \sinh[\alpha_1(l+z_b)]$. Performing the distribution,

$$\varphi_1(z_o < z < l, s) =$$

$$\frac{e^{-\alpha_1(z-z_o)}-e^{-\alpha_1(2z_b+z_o+z)}}{2\alpha_1 D_1} + \frac{1}{\beta}\left(\frac{e^{\alpha_1 z}-e^{-\alpha_1(2z_b+z)}}{e^{\alpha_1 l}-e^{-\alpha_1(2z_b+l)}}\right)\sinh[\alpha_1(z_o+z_b)] +$$

$$\frac{1}{2\alpha_1 D_1}\left(\frac{e^{\alpha_1 z}-e^{-\alpha_1(2z_b+z)}}{e^{\alpha_1 l}-e^{-\alpha_1(2z_b+l)}}\right)(e^{-\alpha_1(2z_b+z_o+l)} - e^{\alpha_1(z_o-l)})$$

$$= \frac{\beta\left\{\left(e^{\alpha_1 l}-e^{-\alpha_1(l+z_b)}\right)\left(e^{\alpha_1(z_o-z)}-e^{-\alpha_1(2z_b+z_o+z)}\right)+\left(e^{\alpha_1 z}-e^{-\alpha_1(2z_b+z)}\right)\left(e^{-\alpha_1(2z_b+z_o+l)}-e^{\alpha_1(z_o-l)}\right)\right\}}{+\ 2\alpha_1 D_1(e^{\alpha_1 z}-e^{-\alpha_1(2z_b+z)})\sinh[\alpha_1(z_o+z_b)]} \quad \text{(A45)}$$
$$2\alpha_1 D_1 \beta(e^{\alpha_1 l}-e^{-\alpha_1(2z_b+l)})$$

Factoring out $e^{-2\alpha_1 z_b}$ from the numerator and the denominator,

$$\varphi_1(z_o < z < l, s) = \frac{\beta e^{-2\alpha_1 z_b}\{(e^{\alpha_1(l-z+2z_b)} - e^{-\alpha_1(l+z)}) - (e^{\alpha_1(z-l+2z_b)} - e^{-\alpha_1(l+z)})\} e^{-2\alpha_1 z_b}\left(e^{\alpha_1(z_o+2z_b)} - e^{-\alpha_1 z_o}\right) + 2\alpha_1 D_1 (e^{\alpha_1(2z_b+z)} - e^{-\alpha_1 z}) e^{-2\alpha_1 z_b} \sinh[\alpha_1(z_o+z_b)]}{2\alpha_1 D_1 \beta e^{-2\alpha_1 z_b}(e^{\alpha_1 l} - e^{-\alpha_1(2z_b+l)})}$$

$$= \frac{\beta e^{-2\alpha_1 z_b}\{(e^{\alpha_1(l-z+2z_b)} - e^{-\alpha_1(l+z)}) - (e^{\alpha_1(z-l+2z_b)} - e^{-\alpha_1(l+z)})\}\left(e^{\alpha_1(z_o+2z_b)} - e^{-\alpha_1 z_o}\right) + 2\alpha_1 D_1 (e^{\alpha_1(2z_b+z)} - e^{-\alpha_1 z}) \sinh[\alpha_1(z_o+z_b)]}{2\alpha_1 D_1 \beta (e^{\alpha_1 l} - e^{-\alpha_1(2z_b+l)})} \quad \text{(A46)}$$

Factoring out $e^{\alpha_1 z_b}$ from the denominator,

$$\varphi_1(z_o < z < l, s) = \frac{\beta\left(e^{\alpha_1(l-z)} - e^{\alpha_1-(l-z)}\right)\left(e^{\alpha_1(z_o+2z_b)} - e^{-\alpha_1 z_o}\right) + 2\alpha_1 D_1 (e^{\alpha_1(2z_b+z)} - e^{-\alpha_1 z}) \sinh[\alpha_1(z_o+z_b)]}{4\alpha_1 D_1 \beta e^{\alpha_1 z_b} \sinh[\alpha_1(l+z_b)]} \quad \text{(A47)}$$

In the numerator, recognizing that $2\sinh[\alpha_1(l-z)] = \left(e^{\alpha_1(l-z)} - e^{\alpha_1-(l-z)}\right)$, factoring out $e^{-\alpha_1 z_o}$ from the first term and $e^{-\alpha_1 z}$ from the second term,

$$\varphi_1(z_o < z < l, s) = \frac{2\beta \sinh[\alpha_1(l-z)] e^{-\alpha_1 z_o}\left(e^{2\alpha_1(z_o+z_b)} - 1\right) + 2\alpha_1 D_1 e^{-\alpha_1 z}(e^{2\alpha_1(z+z_b)} - 1) \sinh[\alpha_1(z_o+z_b)]}{4\alpha_1 D_1 \beta e^{\alpha_1 z_b} \sinh[\alpha_1(l+z_b)]} \quad \text{(A48)}$$

Noting that $2e^x \sinh x = e^{2x} - 1$, the numerator becomes,

$$\varphi_1(z_o < z < l, s) =$$

$$\frac{4\beta \sinh[\alpha_1(l-z)] e^{-\alpha_1 z_o} e^{\alpha_1(z_o+z_b)} \sinh[\alpha_1(z_o+z_b)] + 4\alpha_1 D_1 D_1 e^{-\alpha_1 z} e^{\alpha_1(z+z_b)} \sinh[\alpha_1(z+z_b)] \sinh[\alpha_1(z_o+z_b)]}{4\alpha_1 D_1 \beta e^{\alpha_1 z_b} \sinh[\alpha_1(l+z_b)]} \quad \text{(A49)}$$

Cancelling $e^{\alpha_1 z_b}$ and reordering terms, one obtains

$$\varphi_1(z_o < z < l, s) = \left(\frac{\sinh[\alpha_1(z_o+z_b)]}{\alpha_1 D_1 \beta}\right)\left(\frac{\beta \sinh[\alpha_1(l-z)] + \alpha_1 D_1 \sinh[\alpha_1(z+z_b)]}{\sinh[\alpha_1(l+z_b)]}\right) \quad \text{(A50)}$$

Expanding β in the second factor,

$$\varphi_1(z_o < z < l, s) =$$

$$\left(\frac{\sinh[\alpha_1(z_o+z_b)]}{\alpha_1 D_1 \beta}\right)\left(\alpha_1 D_1 \left\{\frac{\sinh[\alpha_1(z+z_b)] + \sinh[\alpha_1(l-z)]\cosh[\alpha_1(l+z_b)]}{\sinh[\alpha_1(l+z_b)]}\right\} + \alpha_2 D_2 \sinh[\alpha_1(l-z)]\right) \quad \text{(A51)}$$

We note that this almost has the same form as Eq (2.21). All that remains is to prove that the quantity in braces is equal to $\cosh[\alpha_1(l-z)]$. Expanding the hyperbolic functions in terms of e,

$$\frac{\sinh[\alpha_1(z+z_b)]+\sinh[\alpha_1(l-z)]\cosh[\alpha_1(l+z_b)]}{\sinh[\alpha_1(l+z_b)]} = \frac{e^{\alpha_1(z+z_b)}-e^{-\alpha_1(z+z_b)}+\frac{1}{2}\left(e^{\alpha_1(l+z_b)}+e^{-\alpha_1(l+z_b)}\right)(e^{\alpha_1(l-z)}-e^{-\alpha_1(l-z)})}{e^{\alpha_1(l+z_b)}-e^{-\alpha_1(l+z_b)}}$$

$$= \frac{e^{\alpha_1(z+z_b)}-e^{-\alpha_1(z+z_b)}+\frac{1}{2}(e^{\alpha_1(2l+z_b-z)}-e^{\alpha_1(z_b+z)}+e^{-\alpha_1(z_b+z)}-e^{-\alpha_1(2l+z_b-z)})}{e^{\alpha_1(l+z_b)}-e^{-\alpha_1(l+z_b)}} \quad \text{(A52)}$$

Re-ordering the terms in the numerator,

$$\frac{\sinh[\alpha_1(z+z_b)]+\sinh[\alpha_1(l-z)]\cosh[\alpha_1(l+z_b)]}{\sinh[\alpha_1(l+z_b)]} = \frac{\frac{1}{2}\left(e^{\alpha_1(2l+z_b-z)}+e^{\alpha_1(z+z_b)}\right)-\frac{1}{2}\left(e^{-\alpha_1(2l+z_b-z)}+e^{-\alpha_1(z_b+z)}\right)}{e^{\alpha_1(l+z_b)}-e^{-\alpha_1(l+z_b)}} \quad \text{(A53)}$$

Factoring out $e^{\alpha_1(l+z_b)}$ from the first term and $e^{-\alpha_1(l+z_b)}$ from the second term of the numerator on the right-hand side,

$$\frac{\sinh[\alpha_1(z+z_b)]+\sinh[\alpha_1(l-z)]\cosh[\alpha_1(l+z_b)]}{\sinh[\alpha_1(l+z_b)]} = \frac{\frac{1}{2}[e^{\alpha_1(l+z_b)}(e^{\alpha_1(l-z)}+e^{-\alpha_1(l-z)})]-\frac{1}{2}[e^{-\alpha_1(l+z_b)}(e^{\alpha_1(l-z)}+e^{-\alpha_1(l-z)})]}{e^{\alpha_1(l+z_b)}-e^{-\alpha_1(l+z_b)}}$$

(A54)

Factoring out $\frac{e^{\alpha_1(l-z)}+e^{-\alpha_1(l-z)}}{2}$ from the numerator on the right-hand side, and recognizing that this is equal to $\cosh[\alpha_1(l-z)]$,

$$\frac{\sinh[\alpha_1(z+z_b)]+\sinh[\alpha_1(l-z)]\cosh[\alpha_1(l+z_b)]}{\sinh[\alpha_1(l+z_b)]} = \cosh[\alpha_1(l-z)]\left(\frac{e^{\alpha_1(l+z_b)}-e^{-\alpha_1(l+z_b)}}{e^{\alpha_1(l+z_b)}-e^{-\alpha_1(l+z_b)}}\right)$$

$$\frac{\sinh[\alpha_1(z+z_b)]+\sinh[\alpha_1(l-z)]\cosh[\alpha_1(l+z_b)]}{\sinh[\alpha_1(l+z_b)]} = \cosh[\alpha_1(l-z)] \quad \text{(A55)}$$

Inserting this into the braces in Eq. (A51) gives,

$$\varphi_1(z_o < z < l, s) = \frac{\sinh[\alpha_1(z_o+z_b)]}{\alpha_1 D_1 \beta}(\alpha_1 D_1 \cosh[\alpha_1(l-z)] + \alpha_2 D_2 \sinh[\alpha_1(l-z)]) \quad \text{(A56)}$$

Expanding β yields,

$$\boxed{\varphi_1(z_o < z < l, s) = \frac{\sinh[\alpha_1(z_o+z_b)]}{\alpha_1 D_1}\left(\frac{\alpha_1 D_1 \cosh[\alpha_1(l-z)]+\alpha_2 D_2 \sinh[\alpha_1(l-z)]}{\alpha_1 D_1 \cosh[\alpha_1(l+z_b)]+\alpha_2 D_2 \sinh[\alpha_1(l+z_b)]}\right)} \quad \text{(A57)}$$

Lastly, re-inserting the expressions for A_1 and B_1 in Eq. (),

$$\varphi_1(0 < z < z_o) = B_1(e^{\alpha_1 z} - e^{-\alpha_1(2z_b+z)})$$

$$= \left(\frac{e^{\alpha_1 z}-e^{-\alpha_1(2z_b+z)}}{e^{\alpha_1 z_o}-e^{-\alpha_1(2z_b+z_o)}}\right)(C_1 e^{-\alpha_1 z_o} + E_1 e^{\alpha_1 z_o})$$

$$= \left(\frac{e^{\alpha_1 z}-e^{-\alpha_1(2z_b+z)}}{e^{\alpha_1 z_o}-e^{-\alpha_1(2z_b+z_o)}}\right)\left(\left[\frac{e^{\alpha_1 z_o}-e^{-\alpha_1(2z_b+z_o)}}{2\alpha_1 D_1} - E_1 e^{-2\alpha_1 z_b}\right]e^{-\alpha_1 z_o} + E_1 e^{\alpha_1 z_o}\right)$$

$$= \left(\frac{e^{\alpha_1 z}-e^{-\alpha_1(2z_b+z)}}{e^{\alpha_1 z_o}-e^{-\alpha_1(2z_b+z_o)}}\right)\left(\frac{1-e^{-2\alpha_1(z_b+z_o)}}{2\alpha_1 D_1} + E_1(e^{\alpha_1 z_o} - e^{-\alpha_1(2z_b+z_0)})\right) \quad \text{(A58)}$$

Factoring out $e^{\alpha_1 z_o}$ from the denominator of the first factor and the second term in the second factor,

$$\varphi_1(0 < z < z_o) = \left(\frac{e^{\alpha_1 z}-e^{-\alpha_1(2z_b+z)}}{e^{\alpha_1 z_o}\left(1-e^{-2\alpha_1(2z_b+z_o)}\right)}\right)\left(\frac{1-e^{-2\alpha_1(z_b+z_o)}}{2\alpha_1 D_1} + E_1 e^{\alpha_1 z_o}(1 - e^{-2\alpha_1(z_b+z_0)})\right) \quad \text{(A59)}$$

Factoring out $1 - e^{-2\alpha_1(z_b+z_o)}$ from the second factor and cancelling

$$\varphi_1(0 < z < z_o, s) = \left(e^{\alpha_1 z} - e^{-\alpha_1(2z_b+z)}\right)\left(\frac{e^{-\alpha_1 z_o}}{2\alpha_1 D_1} + E_1\right)$$

$$= \frac{e^{\alpha_1(z-z_o)}}{2\alpha_1 D_1} - \frac{e^{-\alpha_1(2z_b+z+z_o)}}{2\alpha_1 D_1} + E_1\left(e^{\alpha_1 z} - e^{-\alpha_1(2z_b+z)}\right) \quad \text{(A60)}$$

Looking at Eq (A44), we see that

$$-\frac{e^{-\alpha_1(2z_b+z+z_o)}}{2\alpha_1 D_1} + E_1\left(e^{\alpha_1 z} - e^{-\alpha_1(2z_b+z)}\right) = \varphi_1(z_o < z < l, s) - \frac{e^{\alpha_1(z_o-z)}}{2\alpha_1 D_1} \quad \text{(A61)}$$

Substituting this into $\varphi_1(0 < z < z_o)$,

$$\varphi_1(0 < z < z_o, s) = -\frac{1}{\alpha_1 D_1}\left(\frac{e^{\alpha_1(z_o-z)}-e^{-\alpha_1(z_o-z)}}{2}\right) + \varphi_1(z_o < z < l, s) \quad \text{(A62)}$$

Lastly, inserting the complete expression for $\varphi_1(z_o < z < l, s)$ and recognizing that the term in the parenthesis is equal to $\sinh[\alpha_1(z_0 - z)]$,

$$\boxed{\varphi_1(0 < z < z_o, s) = \frac{\sinh[\alpha_1(z_o+z_b)]}{\alpha_1 D_1}\left(\frac{\alpha_1 D_1 \cosh[\alpha_1(l-z)]+\alpha_2 D_2 \sinh[\alpha_1(l-z)]}{\alpha_1 D_1 \cosh[\alpha_1(l+z_b)]+\alpha_2 D_2 \sinh[\alpha_1(l+z_b)]}\right) - \frac{\sinh[\alpha_1(z_0-z)]}{\alpha_1 D_1}} \quad \text{(A63)}$$

Appendix B: The Limiting Equation

Expanding $\varphi_1(0 < z < z_o, s)$ in terms of e,

$$\varphi_1(0 < z < z_o, s) = \frac{e^{\alpha_1(z_b+z_o)} - e^{-\alpha_1(z_b+z_o)}}{2\alpha_1 D_1}\left(\frac{\alpha_1 D_1\left[\frac{e^{\alpha_1(l-z)} + e^{-\alpha_1(l-z)}}{2}\right] + \alpha_2 D_2\left[\frac{e^{\alpha_1(l-z)} - e^{-\alpha_1(l-z)}}{2}\right]}{\alpha_1 D_1\left[\frac{e^{\alpha_1(l+z_b)} + e^{-\alpha_1(l+z_b)}}{2}\right] + \alpha_2 D_2\left[\frac{e^{\alpha_1(l+z_b)} - e^{-\alpha_1(l+z_b)}}{2}\right]}\right) -$$

$$\left(\frac{e^{\alpha_1(z_o-z)} - e^{-\alpha_1(z_o-z)}}{2\alpha_1 D_1}\right) \quad \text{(B1)}$$

Collecting like terms,

$$\varphi_1(0 < z < z_o, s) = \frac{1}{2\alpha_1 D_1}\left\{\left(e^{\alpha_1(z_b+z_o)} - e^{-\alpha_1(z_b+z_o)}\right)\left[\frac{(\alpha_1 D_1 + \alpha_2 D_2)e^{\alpha_1(l-z)} + (\alpha_1 D_1 - \alpha_2 D_2)e^{-\alpha_1(l-z)}}{(\alpha_1 D_1 + \alpha_2 D_2)e^{\alpha_1(l+z_b)} + (\alpha_1 D_1 - \alpha_2 D_2)e^{-\alpha_1(l+z_b)}}\right] +\right.$$

$$\left. e^{-\alpha_1(z_o-z)} - e^{\alpha_1(z_o-z)}\right\} \quad \text{(B2)}$$

Differentiating with respect to z,

$$\frac{\partial\varphi_1(0<z<z_o,s)}{\partial z} = \frac{1}{2D_1}\left\{\frac{\left(e^{\alpha_1(z_b+z_o)} - e^{-\alpha_1(z_b+z_o)}\right)}{(\alpha_1 D_1 + \alpha_2 D_2)e^{\alpha_1(l+z_b)} + (\alpha_1 D_1 - \alpha_2 D_2)e^{-\alpha_1(l+z_b)}}\left[(\alpha_1 D_1 + \alpha_2 D_2)(-e^{\alpha_1(l-z)}) +\right.\right.$$

$$\left.\left.(\alpha_1 D_1 - \alpha_2 D_2)e^{-\alpha_1(l-z)}\right] + e^{-\alpha_1(z_o-z)} + e^{\alpha_1(z_o-z)}\right\} \quad \text{(B3)}$$

Making the following substitution,

$$D_a = \frac{\alpha_1 D_1 - \alpha_2 D_2}{\alpha_1 D_1 + \alpha_2 D_2} \quad \text{(B4)}$$

Eq (B3) becomes

$$\frac{\partial\varphi_1(0<z<z_o,s)}{\partial z} = \frac{1}{2D_1}\left\{\frac{\left(e^{\alpha_1(z_b+z_o)} - e^{-\alpha_1(z_b+z_o)}\right)}{e^{\alpha_1(l+z_b)} + D_a e^{-\alpha_1(l+z_b)}}\left[D_a e^{-\alpha_1(l-z)} - e^{\alpha_1(l-z)}\right)\right] + e^{-\alpha_1(z_o-z)} + e^{\alpha_1(z_o-z)}\right\} \quad \text{(B5)}$$

Evaluating this expression at $z = 0$ gives

$$\left.\frac{\partial \varphi_1(0<z<z_o,s)}{\partial z}\right|_{z=0} = \frac{1}{2D_1}\left\{\frac{\left(e^{\alpha_1(z_b+z_o)}-e^{-\alpha_1(z_b+z_o)}\right)}{e^{\alpha_1(l+z_b)}+D_a e^{-\alpha_1(l+z_b)}}[D_a e^{-\alpha_1 l} - e^{\alpha_1 l})] + e^{-\alpha_1 z_o} + e^{\alpha_1 z_o}\right\}$$

$$= \frac{1}{2D_1}\left\{\frac{e^{\alpha_1(z_b+z_o)}\left(1-e^{-2\alpha_1(z_b+z_o)}\right)}{e^{\alpha_1(l+z_b)}\left(1+D_a e^{-2\alpha_1(l+z_b)}\right)}\left[e^{\alpha_1 l}\left(D_a e^{-2\alpha_1 l} - 1\right)\right] + e^{-\alpha_1 z_o} + e^{\alpha_1 z_o}\right\}$$

$$= \frac{1}{2D_1}\left\{\left[\frac{1-D_a e^{-2\alpha_1 l}}{1+D_a e^{-2\alpha_1(l+z_b)}}\right](e^{-\alpha_1(2z_b+z_o)} - e^{\alpha_1 z_o}) + e^{-\alpha_1 z_o} + e^{\alpha_1 z_o}\right\} \quad \text{(B6)}$$

If $2\alpha_1(l + z_b) \gg 1$,

$$\left.\frac{\partial \varphi_1(0<z<z_o,s)}{\partial z}\right|_{z=0} \approx \frac{1}{2D_1}\left\{\left(e^{-\alpha_1(2z_b+z_o)} - e^{\alpha_1 z_o}\right)(1 - D_a e^{-2\alpha_1 l})(1 - D_a e^{-2\alpha_1(l+z_b)}) + e^{-\alpha_1 z_o} e^{\alpha_1 z_o}\right\} \quad \text{(B7)}$$

To first order in D_a,

$$\left.\frac{\partial \varphi_1(0<z<z_o,s)}{\partial z}\right|_{z=0} \approx \frac{1}{2D_1}\left\{\left(e^{-\alpha_1(2z_b+z_o)} - e^{\alpha_1 z_o}\right)\left(1 - D_a\left[\left(e^{-2\alpha_1(l+z_b)} + e^{-2\alpha_1 l}\right)\right]\right) + e^{-\alpha_1 z_o} + e^{\alpha_1 z_o})\right\} \quad \text{(B8)}$$

Carrying out the multiplication and re-arranging,

$$D_1 \left.\frac{\partial \varphi_1(0<z<z_o,s)}{\partial z}\right|_{z=0} = \frac{1}{2}\left(e^{-\alpha_1 z_o} + e^{-\alpha_1(2z_b+z_o)} + D_a[e^{\alpha_1(z_o-2l)} + e^{-\alpha_1(2l+2z_b-z_o)} - e^{-\alpha_1(2l+2z_b+z_o)} - e^{-\alpha_1(2l+4z_b+z_o)}]\right) \quad \text{(B9)}$$

This is the limiting equation and is renamed as $\varphi_1^{(LE)}(0 < z < z_o, s)$ in Eq (3.19) and Eq (3.20)